Chlorite and Epidote Mineral Chemistry in Porphyry Ore Systems: A Case Study of the Northparkes District, NSW, Australia

Adam Pacey[1,2,*], Jamie J. Wilkinson[2,1] and David R. Cooke[3,4]

[1]*Department of Earth Science and Engineering, Imperial College London, South Kensington, London, SW7 2AZ, United Kingdom*

[2]*Department of Earth Sciences, Natural History Museum, Cromwell Road, London, SW7 5BD, United Kingdom*

[3]*Centre for Ore Deposits and Earth Sciences (CODES), University of Tasmania, Hobart, Tasmania 7001, Australia*

[4]*Transforming the Mining Value Chain (TMVC), an Australia Research Council (ARC) Industrial Transformation Research Hub, University of Tasmania, Hobart, Tasmania 7001, Australia*

**Corresponding author: adampacey@gmail.com*

KEYWORDS:

Propylitic alteration, hydrothermal alteration, porphyry deposit, mineral chemistry, chlorite, epidote, Northparkes

ABSTRACT

Propylitic alteration, characterized by the occurrence of chlorite and epidote, is typically the most extensive and peripheral alteration facies developed around porphyry ore deposits. However, exploration within this alteration domain is particularly challenging, commonly owing to weak or non-existent whole rock geochemical gradients, and because similar assemblages can be developed in other geological settings, particularly during low-grade metamorphism. We document and interpret systematic spatial trends in the chemistry of chlorite and epidote from propylitic alteration around the E48 and E26 porphyry Cu-Au deposits of the Northparkes district, NSW, Australia. These trends vary as a function of both distance from hydrothermal centers and alteration paragenesis.

The spatial trends identified in porphyry-related chlorite and epidote at Northparkes include: (1) a deposit-proximal increase in Ti, As, Sb and V in epidote and Ti in chlorite; (2) a deposit-distal increase in Co and Li in chlorite and Ba in epidote; and (3) a pronounced halo around deposits in which Mn and Zn in chlorite, as well as Mn, Zn, Pb and Mg in epidote are elevated. Chlorite Al/Si ratios and epidote Al/Fe ratios may show similar behavior to Mn-Zn or simply decrease outwards, and V and Ni concentrations in chlorite are lowest in the peak Mn-Zn zone. In comparison to porphyry-related samples, chlorite from the regional metamorphic assemblage in the district contains far higher concentrations of Li, Ca, Ba, Pb and Cu, but much less Ti. Similarly, metamorphic epidote contains higher concentrations of Sr, Pb, As and Sb, but less Bi and Ti.

These chlorite and epidote compositional trends are the net result of fluid-mineral partitioning under variable physicochemical conditions within a porphyry magmatic-hydrothermal system. They are most easily explained by the contribution of spent magmatic-derived ore fluid(s) into the propylitic domain. It is envisaged that such fluids experience progressive cooling and reduction in fS_2 during outwards infiltration into surrounding country rocks, with their pH controlled by the extent of rock-buffering experienced along the fluid pathway.

INTRODUCTION

Propylitic alteration is typically the most ubiquitous and laterally extensive alteration facies in porphyry ore systems, as exemplified in the Northparkes district. With mineral exploration increasingly focused on searching under cover, it may be the only visible sign of hydrothermal activity. Consequently, exploration success could be greatly improved given the ability to: (1) vector toward mineralized/hydrothermal centers within propylitically-altered terrain; and (2) differentiate propylitic alteration around ore deposits from the similar assemblages developed during regional metamorphism or other non-mineralizing processes. Measurement of several major and trace elements in the dominant propylitic alteration minerals chlorite and epidote, to document their concentrations and spatial dispersion, can provide such an ability.

Systematic spatial variations in the major element chemistry (Fe, Mg, Mn, Al) of chlorite developed around sulfide orebodies have occasionally been documented, but historically received little attention. Price (1953) noted an increasing Fe concentration in chlorite with distance from volcanogenic massive sulfide orebodies

in NW Quebec, Canada. This trend was similarly recorded by Ballantyne (1981) at the North Silver Bell porphyry Cu deposit of Arizona, USA, but could not be proven in the nearby Safford deposit. However, the Mn content of chlorite in both these porphyry systems was shown to systematically increase, then decrease with outwards progression from orebodies across the propylitic alteration zone, producing a Mn in chlorite halo. Norman et al. (1991) further documented distal Fe and Mn enrichment in chlorite from the Southwest Tintic district, Utah, USA. In addition to such trends, the concentration of Al in the chlorite tetrahedral site has been widely recognized as a useful geothermometer (e.g., Cathelineau and Nieva, 1985; de Caritat et al., 1993).

As both chlorite and epidote can accommodate a large range of possible cations (Appendix A), the trace element composition of both these minerals has significant potential to provide spatial compositional trends useful for mineral exploration. With this in mind, Wilkinson et al. (2015) investigated the mineral chemistry of chlorite across the propylitic zone at the Batu Hijau porphyry Cu-Au deposit, Indonesia, and Cooke et al. (2014) investigated variations in epidote chemistry surrounding porphyry and skarn occurrences of the Baguio district, Philippines. Several trends in mineral chemistry were documented. Chlorite demonstrated deposit-proximal elevated Ti, V and Mg contents, a halo of enrichment in Mn and Zn, and a distal increase in the concentration of Sr, Li, Ba and Ca. Epidote typically contained highest concentrations of As, Sb, Pb, Zn and Mn in more deposit-distal locations, >1.5 km from zones of potassic alteration. Studies based on the Collahuasi district of Chile (Baker et al., this volume), Resolution in Arizona (Cooke et al., this volume) and El Teniente in Chile (Wilkinson et al, this volume) build upon this work. For epidote they demonstrate how mineral chemistry can potentially provide an indication of fertility for porphyry-type ore deposits and act as a discriminator between different epidote-bearing alteration domains. Similarly, at Resolution and El Teniente, these studies highlight the utility and consistency of spatial trends in chlorite mineral chemistry as a potentially powerful vectoring tool toward porphyry centres.

However, spatial trends in the composition of chlorite and epidote are not only useful for exploration, they also record the behavior and dispersion of many elements as a consequence of changing physicochemical conditions across the propylitic facies. Understanding what controls element dispersion within this facies is therefore the first step in determining the conditions under which it occurs, and ultimately the source of the

alteration fluid itself. It is also necessary to provide a rationale for the routine use of particular elements in exploration.

In this paper we document systematic spatial variation in the mineral chemistry of chlorite and epidote across the propylitic alteration zones surrounding the Endeavour (E)48 and E26 deposits in the Northparkes district of NSW, Australia. Further, we compare results to the regional, post-mineralization, metamorphic assemblage. To facilitate this, a comprehensive suite of well-constrained samples was collected over a wide area, ranging from 300 m to 25 km distant from the porphyry orebodies.

Major element compositions were determined by scanning electron microscopy-energy dispersive spectroscopy (SEM-EDS; 7,026 analyses from 107 chlorite and 100 epidote samples). Minor and selected trace element compositions were determined by laser ablation inductively coupled plasma mass spectrometry (LA-ICP-MS; 1,660 analyses from 64 chlorite and 59 epidote samples).

Numerous spatial compositional trends in both chlorite and epidote are defined which are of potentially significant use in exploration. Observed element distribution patterns also allow the major controls on geochemical dispersion and mineralogical residence in the propylitic zone to be inferred.

GEOLOGICAL CONTEXT

The Northparkes district, located in Central West NSW, Australia, is host to a cluster of five silica-saturated and relatively small alkalic porphyry Cu-Au deposits – E22, E26, E27, E48 and GRP314 – that occur in an area of ~10 km^2 (Fig. 1). The total remaining measured, indicated and inferred resource is 472 Mt at 0.56% Cu and 0.19 g/t Au (Pacey et al., 2019a).

Country rocks in the district are dominated by volcanic and volcaniclastic lithologies with local intercalations of shallow-water marine sediments (Krynen et al., 1990; Simpson et al., 2005). Three major stratigraphic packages are recognized: the Nelungaloo (Early Ordovician), Goonumbla (Mid-Late Ordovician) and Wombin Volcanics (Late Ordovician to earliest Silurian). Igneous rocks within these groups record evolution from basalts through trachyandesites to trachytes respectively (Pacey et al., 2019a) and are typically considered

to represent magmatism as part of the postulated Macquarie Island Arc (e.g., Glen et al., 1998; Glen et al., 2012).

Mineralization-related intrusive rocks appear broadly comagmatic with the Wombin Volcanics and, based on geochronology data, constrain magmatic-hydrothermal activity as Late Ordovician-earliest Silurian (Lickfold et al., 2007). The most voluminous intrusion at Northparkes is a stock which varies locally in composition from an equigranular biotite quartz monzonite to plagioclase-phyric alkali feldspar granite and underlies much of the mining area. This stock is host to a later, and variably feldspar-phyric, quartz monzonite intrusive phase which it appears to entirely enclose (Fig. 2B; Pacey et al., 2019a). Both these igneous bodies are sharply cut by a complex series of quartz monzonite porphyry pipes and dikes to which mineralization is spatially and temporally linked (Heithersay and Walshe, 1995; Lickfold et al., 2003; Pacey et al., 2019a).

The quartz monzonite porphyry complexes are typically only ~50-100 m in diameter but extend to depths of >1 km (Fig. 2). Such pipe-like morphology has led some workers to suggest their emplacement was localized at the intersection of broadly NE-SW- and NW-SE-trending fault-fracture sets (Harris, 1997; Crawford, 2001). Based on textural evidence, Pacey et al. (2019a) consider the quartz monzonite porphyry complexes as original low-viscosity, yet crystal-rich, silicate melt-aqueous fluid slurries that record the discharge of magmatic fluids. Each intrusive center appears to have generated its own magmatic-hydrothermal system. Intense and pervasive potassic (K-feldspar) alteration and local quartz vein stockworks, both accompanied by Cu sulfide mineralization, are exclusively observed within and around the apices of the quartz monzonite porphyry complexes. This alteration-mineralization transitions, with increasing distance from deposit centers, through an intermediate biotite ± magnetite facies into a widespread barren propylitic (epidote-chlorite) assemblage (Figs. 1-2). Pacey et al. (2019a) documented how the intensity of propylitic alteration varies largely as a result of both overall distance to the deposits (and on a smaller scale distance from vein centers; distal = weaker) and permeability (lower lithological or fracture-controlled permeability = weaker).

Late- to post-mineralization monzonite porphyry intrusions are also recognized at Northparkes. One particularly distinctive, crystal-crowded phase occurs as SE-striking dikes and is often referred to as the ‘Zero’ porphyry, due to its low Cu-Au concentrations (<10 ppm Cu, <1 ppm Au) which result in local grade dilution

(Lickfold et al., 2003; Pacey et al., 2019a). A significant post-mineralization feature in the district is the Altona Fault, a large, shallowly (~15°) east-dipping planar structure with an unknown displacement that truncates the top of the E48 and GRP314 deposits (Fig. 2).

METHODOLOGY

Sample collection and preparation

Samples of chlorite and/or epidote were collected from diamond drill core to provide almost continuous, and where possible sub-horizontal, transects across the propylitic alteration halo either side of the E48 and E26 deposits (Figs. 1 and 2). As propylitic alteration extends beyond the limit of diamond drilling, several small samples (≤1 cm) were also collected from appropriate rock chip drillholes which penetrated through surficial cover in the immediate vicinity of the deposits. The majority of sampling was conducted below the level of the Altona Fault (Fig. 2) to ensure an undisturbed relationship between alteration and mineralization. Thus, samples are concentrated in the footwall, to the east of both deposits. For comparison, samples of chlorite and epidote associated with post-mineralization regional metamorphism were also collected from district outcrops, largely to the south of the Northparkes Mines, where its effect is most obvious.

The most appropriate area (ideally containing abundant, coarse grained epidote and chlorite) of each diamond drill core and outcrop sample was selectively cut out and mounted into a 25 mm diameter, polished resin block. Rock chip samples were cut in two to provide flat surfaces and similarly mounted.

Distinction of metamorphic samples

Metamorphic strain is partitioned in the region, with the mining area showing very limited deformation, thought to be a result of the underlying, rigid biotite quartz monzonite pluton acting as a coherent crustal block (e.g., Scheibner, 1993). Further, there is no evidence to suggest alteration assemblages at Northparkes were overprinted or modified during metamorphism. The field distinction between deposit-related propylitic alteration and regional metamorphism in this district is therefore mostly straightforward: the magmatic-hydrothermal and metamorphic domains are, for the most part, spatially separated and usually present unique and contrasting characteristics.

The propylitic facies is typically heterogeneous and shows a close relationship to veins that are usually surrounded by intense and texturally-destructive alteration halos. Epidote of medium grain size (grains visible under a 10x hand lens and occasionally to the naked eye) is abundant and pyrite is also common. The surrounding rock is consistently hematite-reddened. K-feldspar, chalcopyrite and anhydrite (around E26 and GRP314 only) may be present in minor quantities; prehnite and pumpellyite were not observed. By comparison, the metamorphic assemblage is far more pervasive and homogeneous, dominated by chlorite with prehnite, pumpellyite and, more rarely, fine-grained epidote; veins are infrequent. Although significant epidote was documented occurring along a fault in the Nelungaloo Volcanics, no sulfides were observed and no alteration halo surrounds the structure.

Based on these differences, samples NP13AP253 and NP13AP255 would be classified as metamorphic. However, the latter is close to the 'Nash's Hill' prospect (a small area of advanced argillic alteration of unknown origin) and adjacent samples (NP13AP264, NP13AP265 and NP13AP270) are classified as propylitic (Fig. 1). Hence, these two samples, although somewhat ambiguous, were preliminarily classified as propylitic.

Mineral analyses

A complete account of the analytical and data reduction procedures is provided as Appendix B, with only a brief overview given here.

Prepared samples were initially viewed under SEM using back-scattered electron (BSE) imaging and analyzed where appropriate via SEM-EDS. Use of a SEM was essential in order to obtain major element mineral chemistry data, observe alteration textures (Appendix C) and check the suitability of samples for subsequent analysis via LA-ICP-MS. Ultimately, major element SEM-EDS data were acquired for 3,213 chlorite grains (from 108 of 125 samples) and 3,856 epidote grains (from 100 of 125 samples). A total of 64 samples contained chlorite, and 59 contained epidote suitable for LA-ICP-MS analysis (Figs. 1 and 2).

Epidote and chlorite were analyzed separately via LA-ICP-MS, each for a particular set of elements selected based on their potential for substitution into the crystal lattice (Appendix A), abundance in the hydrothermal system or sensitivity to inclusions/contaminant phases. In total 1,470 ablation signals were obtained from 64 chlorite samples, and 1,249 ablation signals were obtained from 59 epidote samples, giving an average of 22

spot analyses in each mineral sample. Rigorous manual processing, quantification and filtering of LA-ICP-MS data was conducted to ensure results only reflect the ablation of clean, uncontaminated mineral. In total, 924 chlorite analyses and 736 epidote analyses were retained from the initial acquired dataset, representing a quality control rejection rate of 37% and 41% respectively.

RESULTS

Sample information, SEM-EDS and LA-ICP-MS compositional data are tabulated in Appendix C. Results are presented graphically for consideration in the following text. For reference, a brief review of chlorite and epidote mineralogy is also provided as Appendix A.

Chlorite composition

Based on the calculated atomic abundances of Fe, Mg and Mn per formula unit (Appendix C), the chlorite analyzed is almost exclusively clinochlore (Fig. 3A). Fe/(Fe + Mg) ratios are typically in the range 0.3-0.4 with Si largely between 2.8-3.2 atoms per formula unit (apfu). Thus, most analyses are further classified as pycnochlorite utilizing the scheme of Hey (1954). An average formula for samples from deposit-related propylitic alteration is $(Mg_{2.91}Fe_{1.66}Mn_{0.13}Al_{1.22})[(Al_{1.09}Si_{2.91})O_{10}](OH)_8$ and for regional metamorphic samples is $(Mg_{2.77}Fe_{1.89}Mn_{0.07}Al_{1.17})[(Al_{1.04}Si_{2.96})O_{10}](OH)_8$, using 2,870 and 343 SEM-EDS analyses respectively. These calculations assume all Fe is Fe^{2+} and are based on 28 oxygen equivalents per formula unit. Although Fe^{2+}/Fe^{3+} cannot be directly measured through SEM-EDS or LA-ICP-MS, estimates of Fe^{3+} and Fe^{2+} in chlorite were calculated based on stoichiometry (Appendix C) and indicate Fe^{3+} rarely exceeds 0.1 apfu in all samples, with an average of 0.07 apfu.

All samples demonstrate an excellent negative correlation between Si and Al (Fig. 3B) attributable to the variable substitution of these cations for one another. Similarly, a strong negative correlation exists between Fe + Mg and Mn, although many samples plot slightly below the obvious linear correlation (Fig. 3C), indicating the presence of other cations in the M^{2+} octahedral site below detection of SEM-EDS. It is further evident that an increase in the Mn content of chlorite is broadly associated with an increase in the Fe/Mg ratio and this relationship may be linear within particular samples (Fig. 3D). This perhaps suggests Mn preferentially substitutes for Mg, or an increased Fe content favors incorporation of Mn over Mg, or vice versa.

Total Fe + Mg + Mn is negatively correlated with Si + Al (Fig. 3E), reflecting the overall limit of cations which can be accommodated per formula unit. Individually, increasing total Al (and thereby decreasing Si) is associated with a general reduction in Mg (Fig. 3F) but simultaneous increase in Fe (Fig. 3G) and the amount of Mn (Fig. 3H) which can be incorporated into the structure, demonstrating the complex interplay between all major cations.

The Ti content of chlorite, as determined by LA-ICP-MS, shows a positive logarithmic correlation with calculated tetrahedral Al (Fig. 3I; R^2 = 0.5) and thereby simultaneous negative correlation with Si (Fig. 3J; R^2 = 0.5). Most simply this suggests Ti^{3+} also directly substitutes for Si^{4+}.

The concentrations of Na and K are typically <200 ppm and <500 ppm, averaging 100 ppm and 200 ppm respectively. Silver, Bi and Cr are almost exclusively <LOD. Cerium, La and U are <LOD in many analyses but, where detected, they are typically <0.2 ppm averaging 0.1 ppm. Tin, Y and Zr are usually above the LOD but have very low concentrations, with Y mostly <1.5 ppm and averaging 0.4 ppm, Zr <2 ppm averaging 0.9 ppm and Sn <2 ppm averaging 1 ppm. None of these elements (Na, K, Ag, Bi, Ce, Cr, La, Sn, U, Y, Zr) demonstrate systematic spatial variation in their concentrations or significant differences between propylitic and metamorphic chlorite samples, hence they are not discussed further.

Spatial trends in chlorite chemistry

In order to assess spatial variation in mineral chemistry with reference to known deposits, 2D linear distances to the center of the E26 and E48 orebodies were calculated for relevant samples (Appendix C). Note 2D rather than 3D distances were calculated, as the vertical center of the porphyry systems is unknown - each system being vertically extensive, with a pipe-like morphology, and remaining open at depth (Fig. 2).

Trends associated with the E48 deposit

Samples from drillholes E48D134, E48D147, GD654, E26D360 and E26D361 are closest to the E48 deposit. There is also a clear zonation in the observed alteration and vein intensity, as well as the alteration mineral assemblage, in these drillholes with respect to the E48 deposit center (detailed logging is provided in Pacey et al., 2019a). Further, O-isotope geothermometry (utilizing quartz-chlorite and quartz-epidote pairs) shows a temperature gradient across selected samples from these drillholes, with increasing temperatures toward the center of E48

(Pacey et al., 2019b). As such, it appears that alteration in these drillholes is largely directly related to this deposit. E48 is therefore associated with the largest sample suite and is also the most centrally located deposit relative to the known systems. Consequently, trends in the mineral chemistry of samples from the aforementioned drillholes, together with all intermediate distance rock-chip and distal metamorphic samples are assessed with respect to E48 (Figs. 4 and 5).

Based on SEM-EDS data, Al is present at ~2.2 apfu in deposit-proximal chlorite, gradually increasing with distance until a maximum of ~2.6 apfu Al is accommodated at ~800 m from the deposit; values then decrease back toward ~2.1 apfu out to ~8 km (Fig. 4A). Silicon, being negatively correlated with Al (Fig. 4B), demonstrates the opposite behavior (Fig. 4B). Regional metamorphic chlorite trends toward even lower Al and higher Si contents but are generally indistinguishable from the most distal propylitic samples. The Mn content of chlorite displays a pronounced zonation around E48, reaching maximum values of 0.4-0.5 apfu at ~800 m from the deposit center (Fig. 4C). Metamorphic chlorites are distinguishable by their low Mn contents, typically <0.1 apfu. By contrast, Mg and Fe contents show no clear systematic trends with proximity to E48, being broadly restricted to the range of 2.5-3.5 apfu and 1.4-2.0 apfu respectively. However, metamorphic chlorite is, on average, slightly more Fe-rich and Mg-poor than propylitic chlorite, but with significant scatter (Fig. 4D,E).

Although based on fewer samples, the Mn content of chlorite determined by LA-ICP-MS displays exactly the same spatial trend as determined by SEM-EDS (c.f. Figs. 4C and 5A). Zinc concentrations further define this remarkable halo, increasing systematically from values typically <1,000 ppm in the most proximal and distal samples, up to almost 2,500 ppm in intermediate-distance samples between ~0.6-2 km from the center of E48 (Fig. 5B). Metamorphic samples show low Zn (<1,000 ppm, with most ~600 ppm), similar to the most distal propylitic samples.

The V concentration in chlorite rapidly decreases from ~400 ppm in most proximal samples to ~100 ppm in chlorite located 600-800 m from E48, before gradually increasing to mean values of 300-400 ppm between 2-4 km (Fig. 5C). It then appears to drop off towards metamorphic chlorite compositions of mostly <200 ppm (with the exception of one unusually high sample, NP13AP264, that is particularly close to the Nash's Hill prospect; Fig. 1). The Ni content of propylitic chlorite appears to display mostly random variability between

5-60 ppm and a large within-sample range (Fig. 5D). However, chlorite located between 600-800 m from the E48 center has Ni consistently <20 ppm and displays limited within-sample variability. Metamorphic samples generally have high Ni content, with only one sample containing <20 ppm and none <10 ppm. Notably, both V and Ni reach their lowest concentrations in chlorite at the same distance from E48 as Mn and Zn reach their maximum values.

Titanium in chlorite, with the exception of three samples, decreases almost exponentially from >200 ppm to ~80 ppm with increasing distance from the E48 system (Fig. 5E). The three samples which fall off this trend are located at ~850 m and are not random anomalies. The sample with the highest Ti concentration (~450 ppm) is characterized by particularly intense and texturally-destructive chloritization, developed as part of the largest observed propylitic vein (type P1 of Pacey et al., 2019a). Those of slightly lower Ti concentrations (~250 ppm) were collected immediately adjacent to this vein, suggesting that Ti in chlorite can decrease away from zones of focused fluid flow at various scales. Metamorphic chlorite shows consistently lower Ti concentrations compared to propylitic samples, with values almost exclusively <50 ppm.

The concentration of Sr in metamorphic chlorite is typically slightly higher than in propylitic samples but is not distinctive. Further, there is no systematic spatial variability within the propylitic samples (Fig. 5F).

Copper, Pb and Ba demonstrate almost identical behavior in chlorite (Fig. 5G-I). All these elements, perhaps counter-intuitively, are almost absent (concentrations <<10 ppm) in chlorite developed within 3 km of E48 but may rarely be slightly elevated in the most distal samples. However, within metamorphic chlorite, much higher concentrations are revealed: Cu up to ~900 ppm; Pb up to ~45 ppm and Ba up to ~200 ppm. The only propylitic sample with such elevated concentrations of Cu, Pb and Ba is NP13AP255, located ~6 km from E48 (Fig. 5G-I). This sample also texturally appears most similar to metamorphic samples and was only considered propylitic given its proximity to the 'Nash's Hill' prospect. These results suggest it is actually of metamorphic origin.

Calcium is consistently present in propylitic chlorite in the range of 100-900 ppm and shows no systematic spatial variation (Fig. 5J). As above, sample NP13AP255 with values ~1,000 ppm again appears similar to metamorphic samples, which themselves mostly contain >1,500 ppm Ca and are thus usefully distinguished.

Similarly, the highest concentrations of Li (~200 ppm) are observed in the metamorphic samples (Fig. 5K). Within propylitic chlorite, Li concentrations remain between ~10-60 ppm until >2 km from E48, at which point they begin to systematically increase toward 150 ppm, effectively transitioning into the range of metamorphic samples.

Antimony in chlorite is typically at levels below the limit of detection via LA-ICP-MS. Where quantifiable it is in the range of 10-200 ppb, although it is unknown where the Sb cation would reside within the mineral structure and this may simply represent minor contamination. Nevertheless, Sb displays a noteworthy systematic increase with distance from E48 and discriminates most distal propylitic chlorite from metamorphic chlorite in which Sb concentrations are consistently low or <LOD (Fig. 5L).

The concentration of Co in chlorite also displays a broad continual increase from ~50 ppm in proximal samples out to ~150 ppm in chlorite located >2 km from E48 (Fig. 5M). Metamorphic chlorites have elevated Co, similar to the distal propylitic chlorite. Values <100 ppm typically correspond to chlorite developed within 1.5 km of E48.

Boron is present in the majority of chlorite samples at concentrations of ~6 ppm and reaches up to 12 ppm. Although B concentration appears to increase between 350 to 600 m from E48 there is too much scatter to define any clear spatial trends (Fig. 5N).

Trends associated with the E26 deposit

Samples from drillhole E26D507 appear to be related to the E26 deposit, although there remains the possibility these may have been affected by the nearby GRP314 system. Drillhole E26D460 was driven sub-horizontally from E26 northwards toward E48, with its collar at the same depth as E26D459 (Fig. 2). As such, samples from E26D460 may be related to either or both deposits. The samples from E26D459 are closest to E26 and are assumed to be related to this system. However, propylitic alteration in this drillhole is not particularly well developed in comparison to all other samples.

Because of these complications, mineral chemistry trends relative to E26 are assessed for each hole individually (Fig. 6). As expected from the E48 results, given the close proximity of samples from E26D507, D26D459 and E26D460 to the E26 deposit, the concentrations of Cu, Pb, Ba, Ba, Ca, Li, Sb and Co in chlorite

do not exhibit any clear spatial variations, hence, for brevity, are not shown in Figure 6. Nevertheless, the absolute concentration of these elements is within the same range as those E48 samples located at similar distances from the system center: Ca = 200-800 ppm and Li = 20-100 ppm with Cu typically <5 ppm, Pb <1 ppm, Ba <4 ppm, Sb <0.1 ppm and Co <120 ppm.

Chlorite from E26D507 shows a decrease in Al and corresponding increase in Si content with progressive distance from E26 (Fig. 6A,B). Although this is broadly what is observed at E48 further out, at similar distances to those represented in E26D507 the trend is actually the opposite. Further, Mg and Fe, which did not show consistent spatial variation around E48, appear to increase and decrease respectively with distance from E26 (Fig. 6F,G). This could represent a host rock control over Fe and Mg content, with all samples from E26 almost entirely hosted within the biotite quartz monzonite stock, thus removing this variable and allowing spatial trends to be observed. In comparison, highly variable volcanic and intrusive rocks surround the upper portions of E48.

In agreement with the E48 dataset, the concentrations of Mn and Zn in chlorite from E26D507 increase with distance from E26, whereas V and Ti broadly decrease (Fig. 6E,H). Maximum values of Mn and Zn in chlorite of 0.2 apfu and ~1,400 ppm respectively fall short of the maximum values reached in the halo around E48. However, samples only provide coverage to <850 m from the deposit and this suggests the maximum point of the Mn-Zn halo around E26 is located still further out. Sr in chlorite from E26D507 is only present at low levels (<13 ppm) and, as for E48, shows no clear spatial trends (Fig. 6I). Ni may be said to slightly increase with progression from E26 but this is at best tenuous (Fig. 6J).

Chlorite from drillhole E26D460 initially shows an increasing Al content away from E26, reaching maximum values at ~600 m before starting to decrease; again Si demonstrates the inverse trend (Fig. 6A,B). Similarly, Mn and Zn show broad halos, with maximum concentrations reached between 500-700 m from E26 (Fig. 6C,D). These trends are in agreement with those observed around E48 and as such could be interpreted as entirely reflecting the E26 system. However, the more distal samples in this drillhole are in fact closer to the E48 system (e.g., Fig. 1) and so the Mn data are considered to define an ‘m’-shaped pattern of two halos, with maximum Mn concentrations at 500 and 700 m from E26, returning to lower levels at 600 m (Fig. 6B).

Mg and Fe contents perhaps show this behavior even better, defining distinct 'm'- and 'w'-shaped trends respectively (Fig. 6F,G). The latter cannot be easily interpreted in relation to just E26, but may be easily thought of as the same geochemical characteristics being displayed around each of the two adjoining systems. Remarkably therefore, chlorite from drillhole E26D460 seems to reflect both the E26 and E48 systems between which it was drilled. The Sr concentration of chlorite in this drillhole also appears to show a 'u'-shaped profile, decreasing away from E26 and increasing toward E48 (Fig. 6I). Titanium content again decreases rapidly from E26 and, in keeping with the proximity to hydrothermal centers, remains relatively elevated (>100 ppm) throughout E26D460, although does not increase toward E48 (Fig. 6H). This is likely because these samples are still too distal from the E48 center.

Chlorite from drillhole E26D459, sampling at depth to the west of E26 (Fig. 2B), is consistently anomalous in comparison to all other propylitic samples. Silicon, Al, Mn, Zn, Ti, V and Sr show no spatial trends, while absolute values of Mn and Ti are particularly low, typically <0.12 apfu and <150 ppm respectively (Fig. 6A-E,H,I). Only the Mg and Fe contents of chlorite appear to exhibit spatial variation and as observed in other samples around E26, the former shows a weak tendency to increase with progression from E26 while the latter decreases (Fig. 6F,G).

Trends in drillhole E34D3

The E34 prospect is a circular magnetic anomaly located ~2 km west of E48 and E26: no mineralized quartz monzonite porphyry bodies are presently known (J. Owens, Northparkes Mines pers. comm., 2015). Propylitic alteration is dominant in drillhole E34D3 but there remains the possibility for undiscovered mineralization in this area and the alteration cannot be simply assumed to be related to known deposits, hence mineral chemistry trends are assessed separately (Fig. 7).

Chlorite from E34D3 is directly comparable to other deposit-related samples, with Pb concentrations mostly <0.6 ppm, Cu <5 ppm, Ba <9 ppm, Sr <13 ppm and Ca in the range of 200-600 ppm. Titanium is also present at relatively high levels with many samples >100 ppm, in the range of 50-250 ppm. Although these results immediately indicate prospectivity, alone they do not imply a new system and could simply reflect the nearby known mineralized centers.

Antimony is largely present at <0.12 ppm and Ni concentrations lie between 5-20 ppm (with the exception of NP12AP023 with ~60 ppm Ni from within the 'Mafic Zero'). Such values for Ni and Sb in the E48 dataset were typical of samples located ~0.5-1.5 km from the deposit.

Notably, a fault of unknown offset juxtaposes basaltic trachyandesite against the biotite quartz monzonite stock at ~500 m depth in drillhole E34D3. Associated with it are zones of shearing and sericitic alteration. As such, the relationship between samples either side of this structure is unclear and spatial variation in chlorite chemistry down this drillhole is best considered only at depths >500 m.

Iron and Mn in chlorite from E34D3 average ~1.6 and ~3.0 apfu respectively and display no systematic downhole variation (Fig. 7F,G). Conversely, Al, Mn and Ti initially show a broad increase in concentration down E34D3, reaching peak values at ~1 km hole-depth before decreasing again (Fig. 7A,C,H). Zinc also exhibits this trend once below the aforementioned fault (Fig. 7D). Still, the maximum concentrations of Mn (0.15 apfu), Ti (250 ppm) and Zn (1,000 ppm) reached are lower than in the center of the Mn-Zn halo around E48. Owing to their negative correlation in chlorite, Si shows the inverse trend to that of Al (Fig. 7B).

The V and Li contents of chlorite broadly increase down E34D3 from 800 m onwards (Fig. 7E,J), reminiscent of trends in the E48 dataset and suggesting progression away from a mineralized center. Cobalt though, which might also be expected to show similar behavior based on E48 data, seems to decrease in concentration down this drillhole (Fig. 7I).

Overall, the absolute concentration values for elements in E34D3 chlorite are typical of other samples located at similar distances to the E48/E26 systems and could be interpreted simply as a part of their alteration shell. However, the presence of a distinct down-hole trend in the abundance of Al, Mn, Ti and Zn is not easily explained by this interpretation. Further, peak concentrations of these elements are coincident with the most intense propylitic alteration (between 1-1.3 km down-hole) and the occurrence of minor magnetite veinlets (at ~1.15 km), which perhaps indicate a transition toward magnetite ± biotite alteration. Such trends could easily reflect either: (1) the presence of an undiscovered mineralized center below the drillhole at ~1 km along its length, or; (2) a major fluid conduit (probably from E48) passing within close proximity to the drillhole, again at ~1 km along its length.

Chlorite results summary

The vast majority of chlorite sampled is manganoan clinochlore. For several elements chlorite chemistry demonstrates a remarkable systematic spatial variation in relation to both distance from hydrothermal centers and differing paragenesis (i.e. propylitic alteration vs. metamorphism). Titanium and Al are positively correlated and appear to decrease in concentration away from zones of focused fluid flow represented by both porphyry centers and major veins; Si varies inversely to Al. Around E26, where the host rock is dominated by homogeneous biotite quartz monzonite, chlorite Mg content increases with progressive distance from the deposit. Iron, being inversely correlated, decreases. Manganese and Zn consistently define halos of elevated concentration around the porphyry centers, coincidental with low concentrations of V and Ni. Cobalt, Li and Sb concentrations increase into zones of distal propylitic alteration, remaining at relatively low values within 2 km of known deposits. Propylitic chlorite lacks any appreciable Cu, Pb and Ba, but these elements may reach significantly elevated values in metamorphic chlorite samples from elsewhere in the region. Similarly, Ca is present at relatively low concentrations in deposit-related chlorite by comparison to most metamorphic samples.

Epidote composition

Based on the calculated atomic abundance of Al, Fe and Mn per formula unit (Appendix C), all analyses were of true epidote (Fig. 8A) with $X_{Ep} \geq 0.5$, mostly in the range 0.6-1.1. Those values >1 reflect more than one Fe atom per formula unit. These calculations assume all Fe is Fe^{3+} and are based on 12.5 oxygen equivalents. Aluminium and Fe demonstrate an expected excellent negative correlation across all values of X_{Ep} (Fig. 8B), suggesting a complete solid solution exists within this range. Further, Fe does not show any linear correlation with Ca (Fig. 8C). These relationships are consistent with Fe being present entirely as Fe^{3+}, or, if present as Fe^{2+}, that it substitutes for Al in the octahedral M sites.

The abundance of Mn shows no clear relationship to the absolute concentrations of Fe, Al or Al+Fe (Fig. 8D), but rather demonstrates a negative correlation with Ca (Fig. 8E). This is strong evidence that Mn is present as Mn^{2+}, substituting for Ca in A sites (likely A1), as opposed to the more typical trivalent behavior and substitution for Al or Fe (e.g., Dollase, 1969, 1973; Ferraris et al., 1989). Accordingly, compositions are driven toward manganoan epidote rather than piemontite. The diffuse nature of the trend also shows that for any

given abundance of Ca there is still a large and variable range in associated Mn content, indicating that other cations must also substitute for Ca when Mn content is low, such that total A site occupancy ≈ 2.0-2.1 apfu.

Using these inferred occupancies, an average formula for samples from deposit-related propylitic alteration can be given as $(Ca_{1.99},Mn_{0.03})(Al_{2.15},Fe_{0.83})Si_{3.00}O_{12}(OH)$ and for regional metamorphic samples as $(Ca_{1.97},Mn_{0.01})(Al_{2.13},Fe_{0.87})Si_{3.01}O_{12}(OH)$, calculated from 3,540 and 316 SEM-EDS analyses respectively (treating Mn <LOD as zero). Therefore, with regard to major element composition, these epidotes of differing paragenesis are almost indistinguishable apart from the slightly higher Mn in propylitic samples.

Total A site cations (Ca + Mn) show a broad negative correlation with total M site cations (Fe + Al), suggesting an overall structural limit of ~5.0 apfu in these sites and a complementary relationship between the two (Fig. 8F). Similarly, Si which dominates the tetrahedral (T) site, is negatively correlated with Fe + Al such that total M+T site occupancy is limited to ~6.0 apfu (Fig. 8G). In contrast, there is no correlation between Si and Ca + Mn, implying M sites provide the link between total A and T site occupancy. This is in agreement with the known crystal structure in which octahedral chains containing the M sites are responsible for the generation of the A and T sites which are formed in-between them (Appendix A).

Generally, there is a tendency for increased Fe/Al ratios to be associated with higher Mn and lower Ca contents (Fig. 8H,I). However, the scattered nature of these trends is more indicative of geochemical/spatial coincidence rather than a crystallographic control, i.e. conditions under which Mn is elevated also favor Fe/Al ratios ≈ 0.3-0.4.

The concentrations of Au, Ag, Tl, Ta, Lu, Hf, and Th are almost exclusively <LOD. Where detected, Hf, Th and Lu average 0.2 ppm whereas Tl and Ta average 0.4 ppm. Sodium and K are frequently <LOD, and, where detected, are typically just above the LOD at <20 ppm and <50 ppm respectively. Similarly, Cu was only detected by LA-ICP-MS in 9% of epidote analyses and Mo in only 25%; typified by concentrations <6 and <0.8 ppm respectively. Europium and Yb are mostly present at <4 ppm averaging 1 ppm; Y <40 ppm averaging 7 ppm; Zr <10 ppm averaging 2 ppm; U <1 ppm averaging 0.4 ppm. None of these elements demonstrate systematic spatial variation in their concentration, or significant differences between propylitic and metamorphic epidote samples, hence they are not discussed further.

Spatial trends in epidote mineral chemistry

Spatial variations in the mineral chemistry of epidote are assessed in the same way as for chlorite.

Trends associated with the E48 deposit

Based on SEM-EDS data (Fig. 9), the Mn content of epidote displays the largest spatial variation, showing a halo of maximum values (~0.15 apfu) at ~800 m from the center of E48 (Fig. 9C), coincident with the Mn-Zn halo observed in chlorite. However, in contrast to chlorite, the epidote Mn halo is defined only by the high concentrations in a given sample (e.g., mean + 1σ values, the upper limit of boxes in Fig. 9C), with nearly every sample also containing a range of Mn contents down to <LOD (although <LOD data points are omitted from Fig. 9C for clarity). This is presumably a direct result of the partitioning of Mn into various crystallographic zones within a single epidote grain. Across the Mn halo, Ca shows a spatially coincident decrease in concentration (Fig. 9B), albeit less well-defined, as a result of the negative substitution correlation between the two elements (Fig. 8E).

Despite much scatter in the data, Al also appears to gradually increase from ~2.1 apfu in deposit-proximal epidote to ~2.3 apfu at ~800 m from E48, before decreasing back to ~2.1 apfu several km from the deposit (Fig. 9E). Again, this trend was observed for Al in chlorite. The inverse trend is observed for Fe in epidote (Fig. 9D) as a consequence of the clinozoisite substitution relationship between the two (Fig. 8B). The Si content of epidote is remarkably uniform throughout all propylitic samples but does show a distinct increase in some of the metamorphic examples (Fig. 9A).

The Mn halo in propylitic epidote based on LA-ICP-MS data (Fig. 10A) is far clearer and better defined than in SEM-EDS data, despite fewer overall samples, because the lower limit of Mn concentrations is still >LOD via this technique. As observed for chlorite, Zn concentration also shows a broadly spatially coincident halo of elevated values (Fig. 10B). Notably, in chlorite, Mn and Zn reached peak concentrations of ~40,000 ppm and ~2,000 ppm, far higher than in epidote where they peak at ~12,000 ppm and ~30 ppm respectively. In contrast, Pb, which was typically <2 ppm in propylitic chlorite, is present in the range 10-150 ppm in propylitic epidote, with nearly all samples located <1 km from E48 containing >60 ppm Pb (Fig. 10C). Metamorphic epidote reaches yet higher Pb concentrations, up to 200 ppm, and rarely displays values <50 ppm.

Magnesium is present in all propylitic epidote samples in the range ~200-1,200 ppm, demonstrating a tendency for concentrations >800 ppm within 1.5 km of E48 (Fig. 10D). In comparison, two of the three metamorphic samples for which LA-ICP-MS data could be obtained contain <200 ppm Mg.

Titanium was also detected in all epidote samples and, as for chlorite, shows a decrease in concentration with distance from E48 (Fig. 10E); proximal samples reach ~2,500 ppm Ti compared to only ~500 ppm in metamorphic epidote. Like Mn, Ti was found to display compositional variation during analysis, probably as a result of growth zoning, producing a large range of Ti concentrations in any given mineral grain. Consequently, this trend is defined only by the maximum Ti concentrations in a given sample.

Bismuth was only present at concentrations >LOD in 43% of analyses and, where quantified, is typically <0.5 ppm. Remarkably, however, Bi reaches ~1-4 ppm in several epidote samples located within 1.5 km of E48, appearing to provide a very useful proximal fertility indicator and metamorphic discriminant (Fig. 10F). Similarly, although V is consistently present between ~10-700 ppm, concentrations of ~700-2,500 ppm are essentially restricted to epidote developed within ~700 m of E48 (Fig. 10G). The absolute abundance of V in epidote is also far higher than in chlorite, which is typically <400 ppm.

Unlike chlorite, in which Sr was usually <40 ppm, propylitic epidote is characterized by Sr concentrations between 200-5,000 ppm, although no pronounced spatial trends are developed (Fig. 10H). Nonetheless, Sr content is a very useful discriminator between propylitic and metamorphic samples in the Northparkes district, with the latter characterized by 5,000-20,000 ppm Sr.

Despite geochemical similarities to Sr, Ba is of only limited abundance (mostly <20 ppm) in all analyzed epidote (Fig. 10I), probably owing to its particularly large ionic radius. Still, the Ba content of epidote does (with the exception of three deposit-proximal samples that show a sharp decrease) appear to erratically increase from <5 ppm within 1 km of E48, up to 5-20 ppm further out. Metamorphic samples contain fairly unremarkable Ba contents in the range ~0-10 ppm.

Arsenic and Sb were detected in the majority of analyzed epidote and demonstrate similar behavior to one another. Generally, concentrations are typically <10 ppm, with most epidote encountered either <1 km from E48 or in metamorphic samples containing >10 ppm As and Sb (Fig. 10J,K). Indeed, compared to all propylitic

samples, As in metamorphic epidote is highly enriched, with values in the range of ~20-100 ppm. Notably, some epidote samples display a large range of As and Sb concentrations, whereas other spatially adjacent samples show only a limited range. Such behavior though shows no correlation with host lithology, epidote texture, or mode of occurrence.

Propylitic epidote mostly contains <2 ppm Co, far lower than observed in chlorite which reached ~150 ppm. Generally, those epidote samples with lowest Co content (~0.5 ppm) are located ~1 km from E48, and more proximal than this, there is a suggestion of a halo feature (Fig. 10L).

Tin occurs at ~1-4 ppm in most samples, including metamorphic epidote. Although there seem to be systematically higher Sn concentrations in epidote located ~0.4-1.5 km from E48 (Fig. 10M), the magnitude of variation is small and is largely dependent on results from only 4-5 samples.

Cerium was also detected in the majority of analyses, usually at concentrations <20 ppm. Of the eight samples in which Ce was >30 ppm, six are located ~0.4 to 1.5 km from E48 and appear to define a proximal enrichment (Fig. 10N).

Trends associated with the E26 deposit

As observed in the E48 dataset, the Si content of epidote from around E26 is remarkably uniform and shows no spatial variability. Copper, Mo and Co are again typically present only at low concentrations of <3, <0.75 and <1.5 ppm respectively. Tin is mostly detected in the range of 1-4 ppm and, in-keeping with the close proximity of most samples to E26, Ba is generally <10 ppm. Despite some E48-proximal epidote containing relatively elevated V (>1,000 ppm) and Ce (>20 ppm) contents, these elements remain below such concentrations in the majority of the E26 epidote analyses. Relatively high concentrations of As (up to ~50 ppm) may be observed, along with Sb (up to ~30 ppm), in agreement with the E48 proximal data, but both are more commonly detected at levels <20 ppm. None of the aforementioned trace elements (Cu, Mo, Co, Sn, Ba, V, Ce, As and Sb) display clear systematic spatial variation with distance to E26 and thus for brevity are omitted from Figure 11.

With increasing distance from E26 the Mn content of epidote in drillhole E26D507 gradually increases (Fig. 11B), as also shown by chlorite along the same transect, thus defining the inner limb of the Mn halo around

the deposit. Given that the increase in Mn is relatively minor (~0.05 apfu), a corresponding, opposite effect on Ca is not observed (Fig. 11A). The Al content of epidote in E26D507 again mimics the trend displayed by chlorite, appearing to decrease with distance (Fig. 11G). Although this trend is in the opposite sense to variation around E48 and in other E26 drillholes, it is created entirely by results from the most distal sample and is probably misleading. As expected, Fe mirrors the trend in Al (Fig. 11F). Unfortunately, it was only possible to obtain LA-ICP-MS data for two epidote samples from E26D507, hence spatial trends cannot be defined for trace elements. Nonetheless, Pb, Zn and Mg concentrations are directly comparable to epidote at similar distances from E48 (Fig. 11C-E), and, once more, Ti is most elevated in the sample closest to E26 (Fig. 11H).

Manganese, Pb, Zn and Mg concentrations in epidote from drillhole E26D460 appear to define a broad halo, reaching peak values 500-600 m from E26 (Fig. 11B-E), with Ca showing inverse behavior to Mn (Fig. 11A). Although such trends could be interpreted purely in relation to E26, as noted for chlorite, distal epidote in this drillhole is closer to E48. Thus, the pattern, in detail, could in fact be speculatively interpreted as an asymmetrical 'm'-shape generated by the overlapping Mn halos of both E26 and E48. This pattern is perhaps also displayed by the Al content of epidote along the drillhole (Fig. 11G). Iron naturally defines the inverse 'w'-shaped trend (Fig. 11F). Titanium concentrations generally decrease from E26 (Fig. 11H) and do not appear to increase toward E48, possibly because the E48 center is still too distant and the marked Ti increase is a proximal phenomenon. The most E26-proximal epidote in E26D460 contains 1-2 ppm Bi (Fig. 11I) which, in the E48 dataset, was seemingly a good indicator of the fertile nature of the hydrothermal system. Strontium is at similar levels (~200-4,000 ppm) to that observed in E48 epidote (Fig. 11J).

The Al content of epidote from drillhole E26D459 displays a systematic increase with progression away from E26 (Fig. 11G). Iron content demonstrates the inverse trend (Fig. 11F), reflecting the negative correlation between these two elements. Such a pattern of increasing Al/Fe with distance was also documented in the E48 dataset across the same distance (to ~800 m) from the deposit, at which point it reversed. This drillhole is the only instance where Al in epidote does not mimic those trends previously identified for Al in chlorite, which did not show any systematic variation in E26D459. However, Fe in chlorite decreases from E26 along

E26D459 in a similar way to the epidote, perhaps suggesting that the incorporation of Fe in epidote is the primary control on Al take-up in this example.

Although Mn and Ca are again inversely correlated in epidote from E26D459, they show no obvious systematic spatial variation in concentration (Fig. 11A,B) and neither do Pb, Zn, Mg and Sr (Fig. 11C-E,J). Titanium and Bi tend to increase with progression from E26, a pattern which is more consistent with a stronger hydrothermal center distal from E26 (Fig. 11H-J). At present, all that can be confidently surmised is that the epidote relates to a fertile system given that Bi concentrations are often >1 ppm.

Trends in drillhole E34D3

Epidote from drillhole E34D3 has typical concentrations of <5,000 ppm Sr, <4 ppm Ba, <9 ppm Sb, <13 ppm As and <0.3 ppm Mo, with Sn in the range 0.5-4 ppm. Copper was never >LOD and although Ce is mostly <25 ppm, two samples contained relatively elevated concentrations, reaching up to 100 ppm. Such characteristics are directly comparable to the deposit-related epidote samples of the E48 dataset located between 0.8-2 km from the system center. Bismuth is <0.5 ppm in most analyses, only reaching >1.5 ppm in one sample.

As observed for chlorite, the Mn content of epidote also increases down E34D3, reaching peak values of ~0.12 apfu at ~0.8 km, then appearing to decrease, at least in terms of maximum values, toward the end of the hole (Fig. 12B). Once again Ca shows the inverse trend (Fig. 12A). Lead is rather erratic but also attains its highest concentrations (>50 ppm) at ~0.8 km (Fig. 12C). Similarly, Ti concentrations reach maximum values toward the middle of the drillhole, broadly corresponding to the region of elevated Mn and Pb (Fig. 12H). Epidote Mg and Co contents show a general reduction in samples up to 1.2 km depth, with Co abundance limited to <0.8 ppm (Fig. 12E,I). Zinc remains largely <20 ppm and V <600 ppm (Fig. 12D,J). Iron and Al display no systematic spatial variation (Fig. 12F,G). Strontium concentrations are typically 300-4,000 ppm (mean 1,200 ppm), thus are indistinguishable from other propylitic epidote samples.

Overall, epidote samples of very similar mineral chemistry to those in E34D3 are located ~0.8-1.5 km from the system center in the E48 dataset. Given the location of E34D3, ~1.5 km from E48, these samples could therefore be interpreted as part of the E48 system. However, as discussed for chlorite, this interpretation does not account for the existence of the halo/peak in Mn and Pb content: this could indicate the existence

of either undiscovered mineralization or a major fluid flow zone/conduit near the drillhole at ~1-1.3 km along its length. Because proximal indicator elements such as Bi and Ti remain relatively low in comparison to the E48 dataset, the latter possibility is considered more likely.

Epidote results summary

All analyses are of manganoan epidote. Grains often show complex internal growth zoning involving variations in Al, Fe, Mn and Ti. However, the Si content is remarkably constant. In comparison to chlorite, epidote shows far higher maximum concentrations of Pb, Sr, Ti, As and Sb, and lower concentrations of Mn, Zn, Cu, Co, Na and K. Copper and Mo do not appear to be readily incorporated into epidote.

Epidote chemistry, as for chlorite, demonstrates systematic spatial variation around known hydrothermal centers and also reflects its paragenesis, either as part of a propylitic or metamorphic assemblage. Manganese, Pb and Zn in epidote define halos of elevated concentration around porphyry deposits, mimicking those observed in the Mn-Zn content of chlorite. Calcium shows inverse trends to those of Mn in this study, thought to be related to competition in the crystal lattice. The maximum concentration of Ti in epidote decreases rapidly away from zones of focused fluid flow and lowest Ti concentrations are in metamorphic epidote. Arsenic and Sb appear to be relatively elevated in both deposit-proximal and deposit-distal epidote, reaching lowest abundances 1-2 km from known mineralization. Bismuth (and V) appear to be useful as fertility indicators, with Bi only detected in the most deposit-proximal epidote (albeit to only limited concentrations). Strontium also discriminates metamorphic epidote very effectively by high concentrations (>5,000 ppm). Similarly, the highest Pb concentrations occur in metamorphic epidote.

CONTROLS ON MINERAL CHEMISTRY IN THE PROPYLITIC ZONE

The chemical composition of chlorite and epidote developed at any point in a hydrothermal system will logically depend upon: (1) the availability of elements, either liberated from the host lithology or supplied by fluids during alteration, hence in turn dependent on fluid source; and (2) fluid-mineral partitioning of cations, that is dependent on which minerals are present/formed as well as the prevailing physical (i.e. temperature, pressure) and chemical (i.e. speciation, pH, fO_2 etc.) conditions. However, it is the prevailing physicochemical conditions and availability of major elements that also determine what minerals are developed in the first

instance. Mineral chemistry is, therefore, the net result of a complex interplay between several key parameters.

Host lithology

In an ideal scenario, to evaluate the possible influence of host rock on mineral chemistry, chlorite and epidote hosted in different lithologies, but otherwise of the same mode of occurrence (vein vs. disseminated) and spatial position would be directly compared. However, in this natural dataset such a rigorous approach was not possible, as various host rocks and alteration intensities are only found in particular locations.

Within the metamorphic environment, a positive correlation between chlorite Fe/Mg and bulk rock composition has been extensively documented (e.g., Foster, 1962; Kawachi, 1975; Bevins and Rowbotham, 1983; Aguirre, 1988; Bevins and Merriman, 1988; Bevins et al., 1991; Robinson et al., 1994; López-Munguira et al., 2002). However, Shikazono and Kawahata (1987) demonstrated that a fluid control (i.e. fluid Fe/Mg, pH, temperature) was the most significant factor in both Kuroko and Neogene Cu-Pb-Zn vein-type deposits of Japan. Prevailing conditions, as well as fluid and rock composition are therefore all capable of influencing the Fe/Mg ratio of chlorite. This is also evidenced in the E48 and E26 chlorite datasets. A systematic spatial trend of decreasing Fe/Mg with progression from the deposit is only observed in the E26 dataset (drillholes E26D507, E26D460 and E26D459) where the majority, or all, samples are hosted within biotite quartz monzonite. In the E48 dataset, where samples span a range of volcanic and intrusive lithologies, no clear spatial trends are observed.

The Fe/Al ratio of epidote also appears to show a minor control by host rock, again only demonstrating systematic spatial trends around E26, where nearly all samples are hosted within biotite quartz monzonite. Similarly, a bulk rock control over the Al/Fe content of epidote in palaeogeothermal systems was proposed by Shikazono (1984). However, this is only one of several factors known to influence the octahedral substitution of Fe^{3+} for Al^{3+} and cannot account for the complex internal zonation of these elements within individual epidote crystals. Thermodynamic analysis (Arnason et al., 1993), experimental investigations (e.g., Holdaway, 1972; Liou, 1973) and observations from other regions (e.g., Raith, 1976; Cavarretta et al., 1980)

strongly suggest that temperature and fO_2 are the most important controls over this substitution, although fCO_2, pH, pressure and fluid composition further affect it to variable extents.

From our dataset it is evident that the major element composition of chlorite and epidote is not exclusive to the host lithology in which they were developed: chlorite and epidote samples from all key rock types are observed throughout the entire spread of the data (Figs. 3 and 8). Considering trace element compositions, in general, the concentrations of most elements in chlorite or epidote are similar across all lithologies within one standard deviation and are usually indistinguishable within two standard deviations. Furthermore, with the exception of Fe/Mg in chlorite and Fe/Al in epidote, all the systematic spatial trends defined in this paper occur on transects across several differing lithological units and, where previously documented, mimic those trends around different porphyry deposits globally.

Therefore, intuitively, the bulk rock composition probably has most influence over chlorite chemistry in the metamorphic environment, where fluid:rock ratios are lowest, there is little to no advection of solutes and lengthy timescales permit extensive fluid-rock equilibrium. In the more fluid-dominant porphyry domain, host lithology is interpreted here as only a second order influence over chlorite and epidote chemistry.

Fluid composition

Systematic spatial variation in the Mn-Zn content of chlorite and Mn-Pb content of epidote define deposit-concentric halos of peak concentrations. These trends are not surprising: base metal geochemical halos are commonly described around porphyry deposits based on whole rock anomalies (e.g., Emmons, 1927; Carson et al., 1976; John, 1978; Chaffee, 1982) and have already been recognized at Northparkes (e.g., Heithersay and Walshe, 1995). Rather than reflecting a pre-existing alteration anomaly, mass balance considerations clearly demonstrate that metasomatic addition of Mn, Zn and Pb occurred during propylitic alteration, with the extent of mass addition proportional to alteration intensity (Pacey, 2016). Chlorite and epidote are both hosts for these elements and thus contribute to, and reflect, this whole rock anomalism.

Because cations such as Mn, Pb and Zn are added during alteration, the maximum concentrations of these elements in chlorite and epidote must partly reflect their original abundance in the alteration fluid, potentially providing fertility indicators. For example, metamorphic chlorite might not be expected to contain

significant quantities of Mn and Zn as metamorphic fluids are unlikely to accumulate these elements to the same concentrations as present in spent/distal porphyry-Cu ore fluids. The presence of Bi in deposit-proximal epidote may also be thought of in this way. However, such interpretations are not straightforward because fluid-mineral partitioning is determined by many other factors, particularly which complexing ligands are present, their abundance, and their stability under given physical conditions. It is the coupled variations in these factors which give rise to the systematic spatial trends observed.

Mineral assemblage

Minerals such as chlorite, epidote, albite, calcite, hematite and pyrite define propylitic alteration and are ubiquitous within propylitically-altered rocks. However, within and across the facies the abundance of each of these minerals may vary significantly. Meanwhile, the composition of any mineral is partly a consequence of preferential element partitioning between the fluid and all phases in the assemblage. Therefore, changing the abundance of one mineral might be expected to change the concentration of elements in other coexisting phases.

In general, the abundance of pyrite, commonly with inclusions of trace chalcopyrite, decreases with progression from porphyry centers and large veins; none was observed in metamorphic samples. Given the strong affinity of Cu, and to a lesser extent Co, for pyrite (e.g., Large et al., 2009; Gregory et al., 2015), this distribution pattern would provide a logical explanation for the lack of appreciable Cu in proximal propylitic chlorite, but relatively high concentrations in metamorphic samples, along with the proximal depletion and gradual but scattered distal increase in Co. Pyrite also readily accommodates As which is again present at highest concentrations in metamorphic samples.

Further, in comparison to chlorite, Pb is incorporated far more easily within epidote and trace sulfides. Hence this could explain the lack of Pb in propylitic chlorite, where coexisting epidote and/or sulfides are abundant, compared to high Pb concentrations in metamorphic chlorite, where only minor epidote is observed and sulfides are absent. Similarly, the Ca content of chlorite is highest in metamorphic samples where Ca-dominant phases, such as calcite and epidote, are less abundant.

The gradual increase in the concentration of Li in chlorite with progression from E48 may likewise reflect a decrease in the abundance of other minerals in which Li is more compatible. This would most probably be mica/phengitic sericite, which is typically observed in samples with intense chloritization.

In light of these interpretations, the relatively low levels of Sr (<40 ppm) in propylitic chlorite, and lack of any spatial variation in chlorite Sr content, might be anticipated given the dominance of albite, calcite and epidote within the assemblage, all of which may host orders of magnitude more Sr (e.g., epidote up to 20,000 ppm). As such, the systematic increase in the Sr content of chlorite documented at the Batu Hijau porphyry Cu-Au deposit (Wilkinson et al., 2015) could, perhaps, simply reflect an outwards decrease in the abundance of epidote, calcite and albite in accordance with the intensity of the alteration.

Cation site occupancy

Where two or more cations have a similar affinity for specific crystal sites within the same mineral, logically they must compete against, and substitute for one another. Certain factors such as temperature, together with the activity of aqueous species, will logically determine how much of each element may be incorporated. The most obvious examples in epidote are Fe-Al and Ca-Mn, and in chlorite Fe-Mg-Mn and Si-Al. Any systematic change in the abundance of one element in such a group generates the inverse trend in the other elements. Without data for two or more minerals containing the same cations it may be difficult to determine which element is driving the change and which are simply compensating.

From our data, all substitutions involving Mn appear to be driven by Mn content, as it shows a spatially coincident halo of elevated concentration in both chlorite and epidote around E48 and E26. Zinc demonstrates identical behavior and does not appear to compete against Mn (c.f. Fig. 5A and B and Fig. 10 A and B), although far higher concentrations of Zn are accommodated in chlorite (1,000s ppm) compared to epidote (10s ppm). In propylitic chlorite, the sudden increase in both Mn and Zn concentrations by 10s of thousand ppm are also correlated with a systematic reduction in V and Ni content, suggesting the latter elements are effectively out-competed for the octahedral M^{2+} chlorite site by the former (c.f. Fig. 5A,B and C,D).

The Fe/Mg ratio of chlorite and Fe/Al ratio of epidote are thought to be partly controlled by host lithology and other variables such as pH (e.g., Arnason et al., 1993). Nevertheless, in chlorite and epidote from the E26 dataset, where samples are dominantly hosted in biotite quartz monzonite, both the Fe/Al ratio of epidote and Fe/Mg ratio of chlorite decrease with distance from E26, suggesting an outwards trend of decreasing Fe is the common driving factor.

Temperature

With increasing distance from a porphyry magmatic center and from large veins (which may permit efficient advection of heat), both the ambient rock temperature and that of the alteration fluid will naturally be expected to decrease.

Temperature is perhaps the most important thermodynamic variable controlling the stability of metal chloride complexes, which are largely responsible for the transport of Cu, Mn, Zn, Pb and Fe in aqueous solution (e.g., Seward and Barnes, 1997; Seward et al., 2014). The stability of all such chloride complexes, and therefore the solubility of associated metal cations, decreases significantly with temperature (as well as during neutralization of acidic pH). Also, under given conditions, the relative stability of these complexes is from $CuCl^+$, the least stable, through $ZnCl^+$, $PbCl^+$ and $MnCl^+$ to $FeCl^+$, the most stable (e.g., Hemley et al., 1992; Hemley and Hunt, 1992; Seward and Barnes, 1997; Kouzmanov and Pokrovski, 2012). As such, outwards cooling of a sulfur-bearing, metal-rich magmatically-derived ore fluid would initially result in supersaturation of Cu sulfides (evidently alongside K-silicate minerals), accounting for the zone of potassic alteration and Cu mineralization. $ZnCl^+$, $PbCl^+$, $MnCl^+$ and $FeCl^+$ complexes would remain stable in solution during this alteration-mineralization. However, with continued infiltration of the fluid into country rocks, cooling and neutralization of any acidic species would eventually result in the sequential destabilization of these complexes. In the case of Fe, this is probably partly responsible for the transition into propylitic alteration, helping to stabilize Fe-bearing minerals such as epidote and chlorite. Zinc, Pb and Mn will either form trace sulfides (dependent on fS_2) and/or substitute wherever possible into the major silicate alteration assemblage. With yet further fluid-rock interaction the abundance of such elements is depleted in the fluid and consequently progressively lower concentrations are present in the propylitic assemblage developed in more distal locations. This is the simplest method of accounting for the observed halo of elevated Mn-Zn-Pb

concentrations in epidote and/or chlorite observed around deposits and strongly suggests a magmatic fluid component within the propylitic domain, as supported independently by field relationships (Pacey et al., 2019a), mass balance constraints (Pacey, 2016) and oxygen and hydrogen stable isotope data (Pacey et al., 2019b).

The extent of Al substitution for Si within the chlorite octahedral site is also largely dependent on temperature (e.g., Cathelineau, 1988; de Caritat et al., 1993). Indeed, a positive correlation between $^{[iv]}$Al and chlorite crystallization temperature is the basis for several empirical geothermometers (e.g., Cathelineau and Nieva, 1985; Kranidiotis and MacLean, 1987; Cathelineau, 1988; Jowett, 1991;) and is also demonstrated by alternative geothermometers based on geologically-calibrated thermodynamic models (e.g. Walshe, 1986; Bourdelle et al., 2013). Application of these various geothermometers to the Northparkes chlorite SEM-EDS dataset yields a range of average formation temperatures (Table 1 and Appendix C). The results from the geothermometers of Cathelineau (1988) and Jowett (1991) are most realistic given constraints imposed by: (1) the observed mineral assemblage; and (2) oxygen isotope geothermometry which shows a transition from ~400^{o}C to ~200^{o}C with outwards progression across the propylitic facies at Northparkes (Pacey et al., 2019b). The equation of Jowett (1991) is preferred overall as it also empirically incorporates the variability in chlorite Fe-Mg content.

The concentration of Ti in chlorite is logarithmically correlated with $^{[iv]}$Al content (Fig. 3I; $R^2 = 0.5$) and hence calculated crystallization temperatures (Fig. 13A). This is in accordance with the observed systematic spatial reduction of Ti concentration in both chlorite and epidote with progression from deposit centers and large veins. Such spatial trends are developed despite the overall immobile behavior of Ti during alteration as evidenced by mass balance (Pacey, 2016). In agreement with Wilkinson et al. (2015), this strongly suggests that, unlike most other elements, the incorporation of Ti into chlorite and epidote is controlled exclusively by temperature and is not sensitive to bulk rock Ti content, mineral partitioning, speciation or aqueous transport. Buffering of chlorite Ti by local excess in the breakdown of biotite, magnetite or other mafic phases to chlorite-titanite/rutile may explain the highly systematic incorporation.

However, in those samples proximal to E48, the expected decrease in both $^{[iv]}$Al and Ti with distance is not observed. Rather Ti concentration decreases away from E48 (Fig. 5E), but Al shows an unusual initial increase to ~800 m before it too finally begins to decrease, effectively defining a subtle halo of elevated Al/Si (Fig. 4A,B). This halo is spatially coincident with maximum Mn-Zn concentrations and, in epidote, most samples also show high Al/Fe ratios (Fig. 9D,E). The latter observation suggests that Al is the common element driving the trend in both minerals. This inverse behavior of Al with respect to Ti in chlorite is responsible for some of the outliers observed in the largely positive correlation between the two elements (Fig. 13A). Consequently, although Ti in chlorite, alteration textures/mineralogy and isotope geothermometry (Pacey et al., 2019b) record a decrease in temperature away from E48, chlorite geothermometry incorrectly suggests a halo of elevated temperatures around the deposit (Fig. 13B). Clearly, some factor other than temperature is both controlling and favoring the partitioning of Al into chlorite and epidote around E48. A reduction in the stability of Al complexes within the hydrothermal fluid could accomplish this. Given that the stabilities of several key Al species are sensitive to pH, a change in pH, itself a result of cooling, is likely responsible for this behavior.

pH

Changes in fluid pH typically have the most significant effect on the concentration of anions such as OH^-, HS^- and HCO_3^-, which are the conjugate base for weak acids. The effect on conjugate bases of stronger acids (e.g., Cl^-, SO_4^{2-}) is often more limited as these acidic species (e.g., HCl, H_2SO_4) are usually already highly dissociated (e.g., Seward and Barnes, 1997; Seward et al., 2014). Regardless, all such anions can be important ligands for particular metal complexes, thus changes in pH will always, to some extent, directly affect their stability and therefore the transport and concentration of metals in aqueous solution.

Acidic pH generally promotes the Cl^- complexing and transport of divalent metal cations, and, in the case of S-bearing fluids, pH may directly control sulfide precipitation. For example, increasing/neutralizing an acidic pH favors the formation of sphalerite:

$$\mathrm{ZnCl_n^{2-n}}(aq) + \mathrm{H_2S}(aq) \Leftrightarrow \mathrm{ZnS}(s) + 2\mathrm{H^+}(aq) + \mathrm{nCl^-}(aq) \qquad \textbf{(Eq. 1)}$$

pH may also control the speciation of metals in aqueous solution. This is particularly important for Al, which is typically present as simple $Al(H_2O)_6^{3+}$ complexes under acidic conditions and as $Al(OH)_4^-$ complexes under

alkaline conditions (e.g., Hem and Roberson, 1967; Brett, 1991; Wesolowski and Palmer, 1994). Both of these complexes are far more soluble than species such as $Al(OH)_2^+$ and $AlOH^{2+}$ which predominate under neutral conditions. Consequently, the total quantity of Al which can be transported in aqueous solution reaches a minimum at near neutral pH (e.g., Hitch et al., 1980; Kinraide, 1991; Wesolowski and Palmer, 1994).

However, pH is only an extensive variable. As such, any systematic spatial trends in mineral chemistry which may be related to pH must be driven by systematic change of an intensive variable, such as temperature, fS_2, fO_2 and/or fluid composition that modifies pH. For magmatically-derived ore fluids rich in dissolved HCl and SO_2, pH may easily be lowered upon progressive cooling of the solution as this leads to increased dissociation of HCl and H_2SO_4 (e.g., Giggenbach, 1992; Rye, 1993). Neutralization of the acidity in such fluids then usually occurs via chemical reaction with the wall rock, typically by the development of muscovite from feldspars (e.g., Eq. 2).

$$3CaAl_2Si_2O_8 + 4H^+(aq) + K^+(aq) + Na^+(aq) \rightarrow KNaAl_4(Al_2Si_6O_{20})(OH)_4 + 3Ca^{2+}(aq) \quad \textbf{(Eq. 2)}$$

As previously highlighted, the Al/Fe ratio of epidote and Al/Si ratio of chlorite both systematically increase with progression from E48, reaching maxima at ~800 m from E48, then decreasing with still further distance, with Al as the common driving factor. Such Al-rich epidote and chlorite samples were collected from zones of particularly intense propylitic alteration (in and around major veins; type P1 of Pacey et al., 2019a) in which the phyllosilicates chlorite and phengitic sericite are predominant, along with quartz, epidote, pyrite and occasional trace sphalerite. Chlorite and epidote from these zones also show some of the highest concentrations of Mn and Zn within the Mn-Zn halo.

These observations suggest that progressive outwards cooling of the alteration fluid during the transition from the potassic to propylitic facies led to a decrease in its pH. Reaction and neutralization with country rock would then produce the observed chloritization and sericitization (e.g., Eq. 2), while conditions would facilitate minor sulfide deposition (e.g., Eq. 1) and favor maximum incorporation of Mn, Zn and Al into the alteration assemblage, as the stability and solubility of their aqueous complexes is reduced. This hypothesis also explains how in disseminated propylitic alteration, developed away from major fluid conduits/veins, the

halo of elevated Al/Fe in epidote and Al/Si in chlorite is not always observed. Cooling alone may generate the zonation in Mn-Zn(-Pb), but pH changes are necessary to account for the systematic behavior of Al. The latter would be minimal in regions where fluid flow was slower as, unlike around major veins, near equilibrium conditions could be maintained with the country rock silicate assemblage, buffering the fluid at a slightly acidic pH.

Pressure

The formation of metal complexes in aqueous solutions is typically associated with a positive change in partial molar volume. Thus, increasing pressure favors the dissociation of complexes into simple hydrated ions, acting to reduce the solubility of metal ions in solution (e.g., Seward, 1981; Seward and Barnes, 1997; Seward et al., 2014). However, the effect of temperature and pH changes on the stability of minerals and aqueous complexes is far more significant, such that pressure changes are unlikely to have had any effect (e.g., Hemley et al., 1986; Rimstidt, 1997; Seward and Barnes, 1997; Mercer and Reed, 2013; Seward et al., 2014). Furthermore, although pressure fluctuations must occur in the center of porphyry systems (during the emplacement of porphyry intrusions and release of (supra)lithostatically pressured fluids) the observed mineral chemistry trends are developed across the peripheral propylitic zone, where such pressure fluctuations are presumably rare and insignificant. The effect of pressure on chlorite and epidote mineral chemistry is therefore considered negligible.

Oxygen and sulfur fugacity

Although spatial changes in the fO_2 and fS_2 of the alteration fluid cannot be precisely determined, the relative variance in these parameters may be inferred based on the observed mineralogical transitions and known phase relationships.

At Northparkes, the abundance of sulfide minerals decreases away from mineralized centers, accompanied by classically-zoned ore mineralogy from deposit-central bornite, through a chalcopyrite shell out to distal pyrite. Such changes clearly reflect an outwards decrease in fS_2 (e.g., Einaudi et al. 2003), in turn probably driven by the progressive saturation and precipitation of sulfide minerals, as a result of fluid cooling (± pH changes).

The abundance of sulfide minerals in the alteration assemblage will inevitably determine the concentration of chalcophile elements incorporated into coexisting silicate minerals such as chlorite and epidote. Copper appears to be sufficiently chalcophile that it is hosted by minor pyrite and trace chalcopyrite throughout the propylitic domain, even at low fS_2, rather than substituting into silicates. Where trace sulfides are absent in the metamorphic domain, chlorite accommodates far higher levels of Cu and Pb, with the latter also elevated in epidote.

Cooke et al. (2014) suggested that fO_2 should decrease away from porphyry magmatic-hydrothermal centers as oxidized fluids (from which sulfate minerals may often be precipitated) are progressively reduced by interaction with country rocks. However, at Northparkes, relatively high fO_2 is implied throughout the magmatic-hydrothermal systems, exemplified not only by the abundance of anhydrite in deposit cores, but also of magnetite, hematite and epidote in the surrounding alteration. The overall zonation in the alteration facies is from deposit-central potassic alteration, with ore grade Cu-Fe-sulfides, through an annulus of magnetite ± biotite alteration and out to propylitic alteration, with much hematite and epidote. With reference to the Fe-S-O system (Hemley et al., 1992) this strongly suggests outwards progression from deposits is accompanied by a gradual increase in fO_2 and concomitant decrease in fS_2. This, however, could be a trait that is restricted to alkalic porphyry deposits, in which hematite reddening is often much more abundant than in calc-alkaline porphyry systems (e.g., Wilson et al., 2007; Bissig and Cooke, 2014; Jago et al., 2014; Micko et al., 2014). Regardless, within the propylitic facies itself, hematite with minor pyrite is ubiquitous and thus it seems unlikely that fO_2 could have varied significantly across this domain. The effect of fO_2 changes on mineral chemistry trends is therefore considered to be negligible.

CONCLUSIONS

Propylitic alteration is the most widespread potential indicator of porphyry-style mineralization. The chemistry of the two most characteristic minerals, chlorite and epidote, has been shown to consistently display systematic variation which reflects both the distance to hydrothermal centers and their formation, either during propylitic alteration or as part of a metamorphic assemblage.

Propylitic chlorite at Northparkes is largely manganoan clinochlore. With increasing distance from mineralized centers: (1) the concentrations of Mn and Zn increase to a maximum and then decrease, defining a halo; Al/Si ratios may show similar behavior or simply decrease outwards, and V and Ni concentrations are lowest in the peak Mn-Zn zone; (2) Ti content decreases, as does the Fe/Mg ratio within host rocks of relatively uniform bulk composition; and (3) the concentrations of Co and Li increase. The Sr concentration of chlorite shows no systematic spatial variation. Metamorphic chlorite contains far higher concentrations of Li, Ca, Ba, Pb and Cu, but much less Ti.

Propylitic epidote at Northparkes is true manganoan epidote. With increasing distance from mineralized centers: (1) Mn, Zn, Pb and Mg define halos of elevated concentration spatially coincident with those of Mn-Zn in chlorite, with an inverse pattern displayed by Ca; (2) the concentrations of Ti, Ba, V, As and Sb decrease, and the Fe/Al ratio may also decrease within host rocks of relatively uniform bulk composition; and (3) apart from a very proximal high, the concentration of Ba increases. Metamorphic epidote contains higher concentrations of Sr, Pb, As and Sb, but less Bi and Ti.

Given data for both minerals, Pb, Sr, Ti, As and Sb preferentially partition into epidote, whereas Zn, Cu, Co, Na and K preferentially partition into chlorite. Copper and Mo are not readily accommodated in epidote. Overall, the maximum Ti contents of chlorite and epidote are an excellent, positively-correlated, proxy for alteration temperature.

Spatial trends in mineral chemistry can be readily explained by the partitioning of elements between the alteration fluid and the stable alteration mineral assemblage under changing physicochemical conditions. With increasing distance from magmatic-hydrothermal centers, the identified trends reflect a decrease in temperature and fS_2 together with the associated influence of such variables on pH and the extent of wall rock interaction. fO_2 may also increase away from deposits based on consideration of the observed mineral assemblage.

The existence of systematic trends in chlorite and epidote chemistry, combined with an understanding of which physicochemical variables control them, has the potential to be utilized as a powerful tool in mineral exploration.

ACKNOWLEDGEMENTS

Thanks are due to AMIRA International, in particular Alan Goode and Adele Seymon, and the industry sponsors of AMIRA project P1060 who provided financial and logistical support for this research. The SEG Foundation Scholarship awarded to AP is also gratefully acknowledged. We are further indebted to Rio Tinto Plc for extra logistical and additional financial assistance. Anton Kearsley, Clara Wilkinson and the late Prof. Teresa Jeffries of the NHM also kindly assisted with SEM and LA-ICP-MS analytical work. AP wishes to extend thanks to Paul Agnew and Debora Araujo of Rio Tinto Plc and all members of the LODE research group at the NHM for their support and encouragement. Finally, we are grateful to Thomas Bissig and Robert Lee for detailed reviews that helped to improve this paper.

REFERENCES

Aguirre, L., 1988, Chemical mobility during low-grade metamorphism of a Jurassic lava flow: Río Grande Formation, Peru: Journal of South American Earth Sciences, v. 1, p. 343-361.

Arnason, J. G., Bird, D. K., and Liou, J. G., 1993, Variables Controlling Epidote Composition in Hydrothermal and Low-Pressure Regional Metamorphic Rocks, *in* Höck, V., and Koller, F., eds., 125 Years Knappenwand Proceedings of a Symposium held in Neukirchen am Grobvenediger (Salzburg/Austria) September 1990, Austria, Abhandlungen der Geologischen Bundesanstalt, p. 17-25.

Baker, M.J., Wilkinson, J.J., Wilkinson, C.C., Cooke, D.R. and Ireland, T.J., 2019, Epidote trace element chemistry as an exploration tool: a case study from the Collahuasi district, northern Chile: Economic Geology, this volume.

Ballantyne, G. H., 1981, Chemical and Mineralogical Variations in Propylitic Zones Surrounding Porphyry Copper Deposits: Unpublished PhD thesis, Utah, USA, University of Utah, 208 p.

Bevins, R. E., and Merriman, R. J., 1988, Compositional controls on coexisting prehnite-actinolite and prehnite-pumpellyite facies assembladges in the Tal y Fan metabasite intrusion, North Wales: Implications for Caledonian metamorphic field gradients: Journal of Metamorphic Geology, v. 6, p. 17-39.

Bevins, R. E., Robinson, D., and Rowbotham, G., 1991, Compositional variations in mafic phyllosilicates from regional low-grade metabasites and application of the chlorite geothermometer: Journal of Metamorphic Geology, v. 9, p. 711-721.

Bevins, R. E., and Rowbotham, G., 1983, Low-grade metamorphism within the Welsh sector of the paratectonic Caledonides: Geological Journal, v. 18, p. 141-167.

Bissig, T., and Cooke, D. R., 2014, Introduction to the Special Issue Devoted to Alkalic Porphyry Cu-Au and Epithermal Au Deposits: Economic Geology, v. 109, p. 819-825.

Bourdelle, F., Parra, T., Chopin, C., and Beyssac, O., 2013, A new chlorite geothermometer for diagenetic to low-grade metamorphic conditions: Contributions to Mineralogy and Petrology, v. 165, p. 723-735.

Brett, C. A., 1991, On the electrochemical behaviour of aluminium in acidic chloride solution: Corrosion Science, v. 33, p. 203-210.

Carson, D. J., Jambor, J. L., Ogryzlo, P., and Richards, T. A., 1976, Bell Copper: Geology, geochemistry and genesis of a supergene-enriched, biotized porphyry copper deposit with a superimposed phyllic zone: Canadian Institute of Mining and Metallurgy Special Volume, v. 15, p. 245-263.

Cathelineau, M., 1988, Cation Site Occupancy in Chlorites and Illites as a Function of Temperature: Clay Minerals, v. 23, p. 471-485.

Cathelineau, M., and Nieva, D., 1985, A chlorite solid solution geothermometer. The Los Azufres (Mexico) geothermal system: Contributions to Mineralogy and Petrology, v. 91, p. 235-244.

Cavarretta, G., Gianelli, G., and Puxeddu, M., 1980, Hydrothermal metamorphism in the Larderello geothermal field: Geothermics, v. 9, p. 297-314.

Chaffee, M. A., 1982, A geochemical study of the Kalamazoo porphyry copper deposit, *in* Titley, S. R., ed., Advances in the Geology of the Porphyry Copper Deposits, Southwestern North America: Tucson, Arizona, University of Arizona Press, p. 211-225.

Cooke, D. R., Baker, M., Hollings, P., Sweet, G., Chang, Z., Danyushevsky, L., Gilbert, S., Zhou, T., White, N., Gemmell, B. J., and Inglis, S., 2014, New Advances in Detecting the Distal Geochemical Footprints of Porphyry Systems - Epidote Mineral Chemistry as a Tool for Vectoring and Fertility Assessments, *in*

Kelley, K. D., and Golden, H. C., eds., Building Exploration Capability for the 21st Century, SEG Special Publication No. 18: Boulder, Colorado, USA, p. 127-152.

Cooke, D.R., Wilkinson, J.J., Baker, M., Agnew, P., Phillips, J., Chang, Z., Chen, H., Wilkinson, C.C., Inglis, S., Hollings, P., Gemmell, J.B., White, N.C., Danyushevsky, L., and Martin, H., 2019, Using mineral chemistry to aid exploration – a case study from the Resolution porphyry Cu-Mo deposit, Arizona: Economic Geology, this issue.

Crawford, A.J., 2001, Tectono-magmatic development of the Ordovician volcanic belts in central western NSW, and the timing and location of porphyry-style mineralisation within the Macquarie Arc, in Crawford, A.J., Cooke, D.R., and Glen, R.A., eds., NSW Ordovician SPIRT report: Hobart, University of Tasmania Centre for Ore Deposit Research, p. 7.41–7.52.

de Caritat, P., Hutcheon, I., and Walshe, J. L., 1993, Chlorite geothermometry: a review: Clays and Clay Minerals, v. 41, p. 219-239.

Dollase, W. A., 1969, Crystal structure and cation ordering of piemontite: American Mineralogist, v. 54, p. 710-717.

Dollase, W. A., 1973, Mössbauer spectra and iron distribution in the epidote group minerals: Zeitschrift für Kristallographie, v. 138, p. 41-63.

Einaudi, M.T., Hedenquist, J.W., and Inan, E.E., 2003, Sulfidation state of fluids in active and extinct hydrothermal systems: Society of Economic Geologists Special Publication 10, p. 285-313.

Emmons, W. H., 1927, Relations of metalliferous lode systems to igneous intrusives: Transactions of the American Institute of Mining and Metallurgical Engineers, v. 74, p. 29-70.

Ferraris, G., Ivaldi, G., Fuess, H., and Gregson, D., 1989, Manganese/iron distribution in a strontian piemontite by neutron diffraction: Zeitschrift für Kristallographie, v. 187, p. 145-151.

Foster, M. D., 1962, Interpretation of the composition and a classification of the chlorites: USGS Professional Paper, v. 414-A, p. 1-33.

Giggenbach, W. F., 1992, Magma Degassing and Mineral Deposition in Hydrothermal Systems along Convergent Plate Boundaries: Economic Geology, v. 87, p. 1927-1944.

Glen, R. A., Quinn, C. D., and Cooke, D. R., 2012, The Macquarie Arc, Lachlan Orogen, New South Wales: its evolution, tectonic setting and mineral deposits: Episodes, v. 35, p. 177-186.

Glen, R. A., Walshe, J. L., Barron, L. M., and Watkins, J. J., 1998, Ordovician convergent-margin volcanism and tectonism in the Lachlan sector of east Gondwana: Geology, v. 26, p. 751-754.

Gregory, D. D., Large, R. R., Halpin, J. A., Baturina, E. L., Lyons, T. W., Wu, S., Danyushevsky, L., Sack, P. J., Chappaz, A., Maslennikov, V. V., and Bull, S. W., 2015, Trace Element Content of Sedimentary Pyrite in Black Shales: Economic Geology, v. 110, p. 1389-1410.

Harris, A.C., 1997, Vein emplacement, E26N porphyry Cu-Au deposit, Goonumbla, New South Wales: Unpublished B.Sc. (Hons) thesis, Brisbane, Australia, University of Queensland, 102 p.

Heithersay, P. S., and Walshe, J. L., 1995, Endeavour 26 North: A porphyry copper-gold deposit in the Late Ordovician shoshonitic Goonumbla Volcanic Complex, New South Wales, Australia: Economic Geology, v. 90, p. 1506-1532.

Hem, J. D., and Roberson, C. E., 1967, Form and Stability of Aluminium Hydroxide Complexes in Dilute Solution: USGS Water Supply Paper, v. 1827-A, p. 1-53.

Hemley, J. J., Cygan, G. L., and d'Angelo, W. M., 1986, Effect of pressure on ore mineral solubilities under hydrothermal conditions: Geology, v. 14, p. 377-379.

Hemley, J. J., Cygan, G. L., Fein, J. B., Robinson, G. R., and d'Angelo, W. M., 1992, Hydrothermal ore-forming processes in the light of studies in rock-buffered systems; I, Iron-copper-zinc-lead sulfide solubility relations: Economic Geology, v. 87, p. 1-22.

Hemley, J. J., and Hunt, J. P., 1992, Hydrothermal ore-forming processes in the light of studies in rock-buffered systems; II, Some general geologic applications: Economic Geology, v. 87, p. 23-43.

Hey, M. H., 1954, A new review of the chlorites: Mineralogical Magazine, v. 30, p. 277-292.

Hitch, B. F., Mesmer, R. E., Baes, C. F., and Sweeton, F. H., 1980, The solubility of Gibbsite (α-$Al(OH)_3$) in 1 molar NaCl as a function of pH and temperature: Oak Ridge National Laboratory Report ORNL-5623, 31 p.

Holdaway, M. J., 1972, Thermal stability of Al-Fe epidote as a function of fO_2 and Fe content: Contributions to Mineralogy and Petrology, v. 37, p. 307-340.

Jago, C. P., Tosdal, R. M., Cooke, D. R., and Harris, A. C., 2014, Vertical and Lateral Variation of Mineralogy and Chemistry in the Early Jurassic Mt. Milligan Alkalic Porphyry Au-Cu Deposit, British Columbia, Canada: Economic Geology, v. 109, p. 1005-1033.

John, E. C., 1978, Mineral zones in the Utah copper orebody: Economic Geology, v. 73, p. 1250-1259.

Jowett, E. C., 1991, Fitting iron and magnesium into the hydrothermal chlorite geothermometer: Geological Association of Canada/Mineralogical Association of Canada/Society of Economic Geologists Joint Annual Meeting Program with Abstracts, v. 16, p. A82.

Kawachi, Y., 1975, Pumpellyite-actinolite and contiguous facies metamorphism in part of upper Wakatipu district, South Island, New Zealand: New Zealand Journal of Geology and Geophysics, v. 18, p. 401-441.

Kinraide, T. B., 1991, Identity of the rhizotoxic aluminium species: Plant and Soil, v. 134, p. 167-178.

Kouzmanov, K., and Pokrovski, G. S., 2012, Hydrothermal Controls on Meta Distribution in Porphyry Cu (-Mo-Au) Systems, *in* Hedenquist, J. W., Harris, M., and Camus, F., eds., Geology and Genesis of Major Copper Deposits and Districts of the World: A Tribute to Richard H. Sillitoe, Society of Economic Geologists Special Publication 16, p. 573-618.

Kranidiotis, P., and MacLean, W. H., 1987, Systematics of chlorite alteration at the Phelps Dodge massive sulfide deposit, Matagami, Quebec: Economic Geology, v. 82, p. 1898-1911.

Krynen, J. P., Sherwin, L., and Clarke, I., 1990, Stratigraphy and structure, *in* Clarke, I., and Sherwin, L., eds., Geological Setting of Gold and Copper Mineralisation in the Parkes area, New South Wales; Records of the Geological Survey of New South Wales 23, p. 1-76.

Large, R. R., Danyushevsky, L., Hollit, C., Maslennikov, V., Meffre, S., Gilbert, S., Bull, S., Scott, R., Emsbo, P., Thomas, H., Singh, B., and Foster, J., 2009, Gold and Trace Element Zonation in Pyrite Using a Laser Imaging Technique: Implications for the Timing of Gold in Orogenic and Carlin-Style Sediment-Hosted Deposits: Economic Geology, v. 104, p. 635-668.

Lickfold, V., Cooke, D. R., Crawford, A. J., and Fanning, C. M., 2007, Shoshonitic magmatism and the formation of the Northparkes porphyry Cu – Au deposits, New South Wales: Australian Journal of Earth Sciences, v. 54, p. 417-444.

Lickfold, V., Cooke, D. R., Smith, S. G., and Ullrich, T. D., 2003, Endeavour Copper-Gold Porphyry Deposits, Northparkes, New South Wales: Intrusive History and Fluid Evolution: Economic Geology, v. 98, p. 1607-1636.

Liou, J. G., 1973, Synthesis and Stability Relations of Epidote, $Ca_2Al_2FeSi_3O_{12}(OH)$: Journal of Petrology, v. 14, p. 381-413.

López-Munguira, A., Nieto, F., and Morata, D., 2002, Chlorite composition and geothermometry: a comparative HRTEM/AEM-EPMA-XRD study of Cambrian basic lavas from the Ossa Morena Zone, SW Spain: Clay Minerals, v. 37, p. 267-281.

Mercer, C. N., and Reed, M. H., 2013, Porphyry Cu-Mo Stockwork Formation by Dynamic, Transient Hydrothermal Pulses: Mineralogic Insights from the Deposit at Butte, Montana: Economic Geology, v. 108, p. 1347-1377.

Micko, J., Tosdal, R. M., Bissig, T., Chamberlain, C. M., and Simpson, K. A., 2014, Hydrothermal Alteration and Mineralization of the Galore Creek Alkalic Cu-Au Porphyry Deposit, Northwestern British Columbia, Canada: Economic Geology, v. 109, p. 891-914.

Norman, D. K., Parry, W. T., and Bowman, J. R., 1991, Petrology and geochemistry of propylitic alteration at Southwest Tintic, Utah: Economic Geology, v. 86, p. 13-28.

Pacey, A., 2016, The Characteristics, Geochemistry and Origin of Propylitic Alteration in the Northparkes Porphyry Cu-Au System: Unpublished PhD thesis, London, UK, Imperial College London, 631 p.

Pacey, A., Wilkinson, J. J., Owens, J., Priest, D., Cooke, D. R., and Millar, I. L., 2019a, The Anatomy of an Alkalic Porphyry Cu-Au System: Geology and Alteration at Northparkes Mines, NSW, Australia: Economic Geology, v. 114, p. 441-472.

Pacey, A., Wilkinson, J. J., Boyce, A. J., and Millar, I. L., 2019b, Isotopic Constraints on the Origin of Propylitic Alteration in Porphyry Deposits: Insights from the Northparkes District, NSW, Australia: Economic Geology, This Volume.

Price, P., 1953, Wall-rock alteration in northwestern Quebec: Geological Society of America Bulletin, v. 64, p. 1464.

Raith, M., 1976, The Al-Fe(III)epidote miscibility gap in a metamorphic profile through the penninic series of the Tauern window, Austria: Contributions to Mineralogy and Petrology, v. 57, p. 99-117.

Rimstidt, J. D., 1997, Gangue Mineral Transport and Deposition, *in* Barnes, H. L., ed., Geochemistry of Hydrothermal Ore Deposits 3rd Edition: New York, John Wiley & Sons, p. 487-515.

Robinson, D., Mazzoli, C., and Primmer, T. J., 1994, Metabasite Paragenesis in South-West England: Proceedings of the Ussher Society, v. 8, p. 231-236.

Rye, R. O., 1993, The evolution of magmatic fluids in the epithermal environment; the stable isotope perspective: Economic Geology, v. 88, p. 733-752.

Scheibner, E., 1993, Structural framework of New South Wales - synthesis: Geological Survey of New South Wales Quarterly Notes, v. 93, p. 1-36.

Seward, T. M., 1981, Metal complex formation in aqueous solutions at elevated temperatures and pressures: Physics and Chemistry of the Earth, v. 13, p. 113-132.

Seward, T. M., and Barnes, H. L., 1997, Metal Transport by Hydrothermal Ore Fluids, *in* Barnes, H. L., ed., Geochemistry of Hydrothermal Ore Deposits 3rd Edition: New York, John Wiley & Sons, p. 435-486.

Seward, T. M., Williams-Jones, A. E., and Migdisov, A. A., 2014, The Chemistry of Metal Transport and Deposition by Ore-Forming Hydrothermal Fluids, *in* Scott, S. D., ed., Treatise on Geochemistry (2nd Edition) Volume 13: Geochemistry of Mineral Deposits, p. 29-57.

Shikazono, N., 1984, Compositional variations in epidote from geothermal areas: Geochemical Journal, v. 18, p. 181-187.

Shikazono, N., and Kawahata, H., 1987, Compositional differences in chlorite from hydrothermally altered rocks and hydrothermal ore deposits: Canadian Mineralogist, v. 25, p. 465-474.

Simpson, C. J., Cas, R. A. F., and Arundell, M. C., 2005, Volcanic evolution of a long-lived Ordovician island-arc province in the Parkes region of the Lachlan Fold Belt, southeastern Australia.: Australian Journal of Earth Sciences, v. 52, p. 863-886.

Walshe, J. L., 1986, A six-component chlorite solid solution model and the conditions of chlorite formation in hydrothermal and geothermal systems: Economic Geology, v. 81, p. 681-703.

Wesolowski, D. J., and Palmer, D. A., 1994, Aluminum speciation and equilibria in aqueous solution: V. Gibbsite solubility at 50°C and pH 3–9 in 0.1 molal NaCl solutions (a general model for aluminum speciation; analytical methods): Geochimica et Cosmochimica Acta, v. 58, p. 2947-2969.

Wilkinson, J. J., Chang, Z., Cooke, D. R., Baker, M. J., Wilkinson, C. C., Inglis, S., Chen, H., and Bruce Gemmell, J., 2015, The chlorite proximitor: A new tool for detecting porphyry ore deposits: Journal of Geochemical Exploration, v. 152, p. 10-26.

Wilkinson, J.J., Baker, M.J., Cooke, D.R., and Wilkinson, C.C., 2019, Exploration targeting in porphyry Cu systems using propylitic mineral chemistry: a case study of the El Teniente deposit, Chile: Economic Geology, this volume.

Wilson, A. J., Cooke, D. R., Stein, H. J., Fanning, C. M., Holliday, J. R., and Tedder, I. J., 2007, U-Pb and Re-Os Geochronologic Evidence for Two Alkalic Porphyry Ore-Forming Events in the Cadia District, New South Wales, Australia: Economic Geology, v. 102, p. 3-26.

Geothermometer	Propylitic chlorite (n = 2,993)	Metamorphic chlorite (n = 220)
Cathelineau (1988)	289	272
Jowett (1991)	290	276
Kranidiotis and MacLean (1987)	160	161
Walshe (1986)	228	220

Table 1 – Average chlorite crystallisation temperatures (°C) based on SEM-EDS analyses (Appendix C) and calculated using the geothermometers referenced; n = number of analyses.

Fig. 1 – Maps of the Northparkes district showing sample distribution and data type acquired relative to known porphyry Cu-Au deposits, prospects and geological features. **(A)** district scale, labelled samples are those discussed individually in text. Inset shows the location of Northparkes within Australia. **(B)** deposit scale, grouped samples are those that were collected from diamond drillholes, as labelled. Geology and alteration features are shown below the level of the Altona Fault (i.e. a plan view at ~780 m below surface). Maps based on GDA94 MGA55, latitude and longitude values are provided as a general guide only.

Fig. 2 – Cross sections for **(A)** E48 and **(B)** E26 between points indicated on Fig. 1B, showing sample distribution and type. Symbology as defined in Fig. 1 and annotated for clarity.

Fig. 3 – Major element chlorite mineral chemistry data from SEM-EDS analyses (n = 3,213), grouped by host lithology. The number of analyses plotted per lithology in A-H is indicated in the legend, in I-J only those analyses with Ti are shown. Data points referred to as 'not shown' are outliers which occur off the scale of the plots. **(A)** chlorite classification, most data plot as clinochlore. **(B-H)** the relationships between major cations within the chlorite structure. **(I-J)** correlations between both calculated tetrahedral Al ($^{[iv]}$Al) and Si with the concentration of Ti, as determined by LA-ICP-MS. Note all data (excluding Ti) are shown in atoms per formula unit (apfu) calculated based on 28 oxygen equivalents.

Fig. 4 – Spatial trends in the composition of chlorite with reference to the center of the E48 deposit, based on SEM-EDS data. Boxes represent the ± 1σ compositional variability in each sample, with whiskers at ± 2σ; circles are outliers >2σ and horizontal lines show the mean value. Blue boxes = propylitic chlorite, grey boxes = metamorphic chlorite; n = number of analyses in which the selected element was >LOD.

Fig. 5 – Spatial trends in the trace element composition of chlorite with reference to the center of the E48 deposit, based on LA-ICP-MS data. Box plots and coloration as for Figure 4.

Fig. 6 – Spatial trends in the composition of chlorite for selected elements with reference to the center of E26, shown individually for each drillhole/transect. Silicon, Al, Mn, Mg and Fe are based on SEM-EDS data, all others on LA-ICP-MS data. Box plots and coloration as for Figure 4.

Fig. 7 – Spatial trends in the composition of chlorite for selected elements along drillhole E34D3 (for location see Fig. 1). Silicon, Al, Mn, Mg and Fe are based on SEM-EDS data, all others on LA-ICP-MS data. Box plots and coloration as for Figure 4.

Fig. 8 – Major element epidote mineral chemistry data from SEM-EDS analyses (n = 3,856), grouped by host lithology. The number of analyses plotted per lithology is indicated in the legend. Data points referred to as 'not shown' are outliers which occur off the scale of the plots. **(A)** classification as true epidote. **(B-I)** relationships between major cations within the epidote structure. Note all data shown in apfu were calculated based on 12.5 oxygen equivalents; Mn values plotting <0.01 apfu are those <LOD via SEM-EDS.

Fig. 9 – Spatial trends in the composition of epidote with reference to the center of the E48 deposit, based on SEM-EDS data. Boxes represent the ± 1σ compositional variability in each sample, with whiskers at ± 2σ; circles are outliers >2σ and horizontal lines show the mean value. Green boxes = propylitic epidote, grey boxes = metamorphic epidote; n = number of analyses in which the selected element was >LOD.

Fig. 10 – Spatial trends in the trace element composition of epidote with reference to the center of the E48 deposit, based on LA-ICP-MS data. Box plots and coloration as for Figure 9.

Fig. 11 – Spatial trends in the composition of epidote for selected elements with reference to the center of E26, shown individually for each drillhole/transect. Calcium, Mn, Fe and Al are based on SEM-EDS data, all others on LA-ICP-MS data. Box plots and coloration as for Figure 9.

Fig. 12 – Spatial trends in the composition of epidote for selected elements along drillhole E34D3 (for location see Fig. 1). Calcium, Mn, Fe and Al are based on SEM-EDS data, all others on LA-ICP-MS data. Box plots and coloration as for Figure 9.

Fig. 13 – Chlorite crystallization temperatures calculated using SEM-EDS data (Appendix C) and the geothermometer of Jowett (1991) compared against: **(A)** chlorite Ti content as determined via LA-ICP-MS (entire chlorite dataset); **(B)** distance to the E48 deposit (E48 dataset only). Each box represents one sample; red boxes = propylitic chlorite, grey boxes = metamorphic chlorite; white boxes in (a) = outlying samples located <800 m from E48, the temperature of which, based on other observations, is likely far higher than suggested by the Jowett (1991) geothermometer.

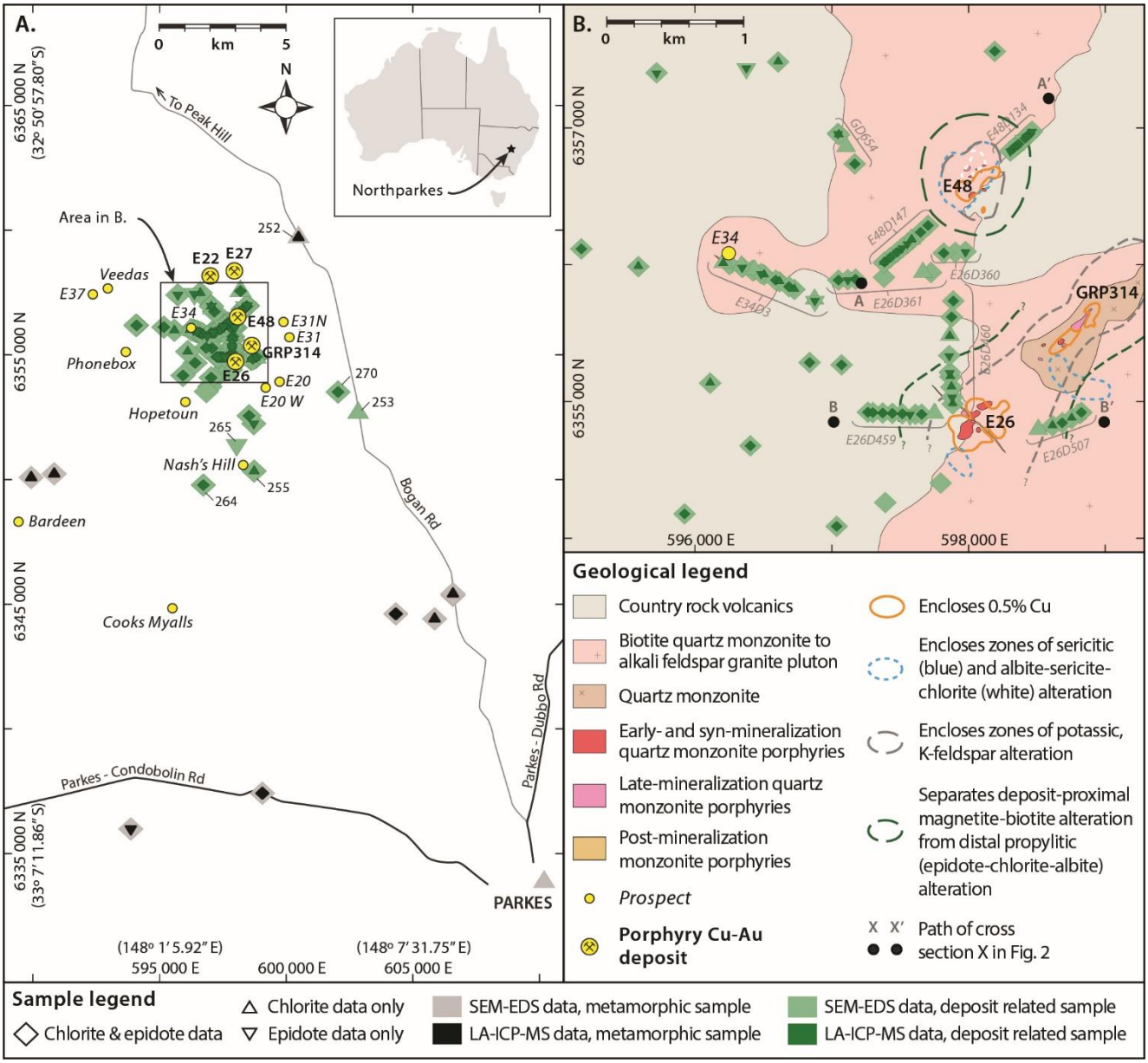
A.
0 km 5
N
To Peak Hill
Northparkes
Area in B.
6365 000 N
(32° 50' 57.80" S)
6355 000 N
6345 000 N
6335 000 N
(33° 7' 11.86" S)
252
E22
E27
Veedas
E37
E34
E48
E31N
E31
GRP314
Phonebox
E26
E20
E20 W
270
253
Hopetoun
265
Nash's Hill
255
264
Bardeen
Cooks Myalls
Bogan Rd
Parkes - Dubbo Rd
Parkes - Condobolin Rd
PARKES
(148° 1' 5.92" E)
595 000 E
600 000 E
(148° 7' 31.75" E)
605 000 E
B.
0 km 1
6357 000 N
6355 000 N
A'
GD654
E48D134
E48
E34
E48D147
E26D360
E34D3
A
E26D361
GRP314
E26D360
B
E26D459
E26
B'
E26D507
596 000 E
598 000 E
Geological legend
Country rock volcanics
Biotite quartz monzonite to alkali feldspar granite pluton
Quartz monzonite
Early- and syn-mineralization quartz monzonite porphyries
Late-mineralization quartz monzonite porphyries
Post-mineralization monzonite porphyries
Prospect
Porphyry Cu-Au deposit
Encloses 0.5% Cu
Encloses zones of sericitic (blue) and albite-sericite-chlorite (white) alteration
Encloses zones of potassic, K-feldspar alteration
Separates deposit-proximal magnetite-biotite alteration from distal propylitic (epidote-chlorite-albite) alteration
X X'
Path of cross section X in Fig. 2
Sample legend
Chlorite & epidote data
Chlorite data only
Epidote data only
SEM-EDS data, metamorphic sample
LA-ICP-MS data, metamorphic sample
SEM-EDS data, deposit related sample
LA-ICP-MS data, deposit related sample

Figure 1

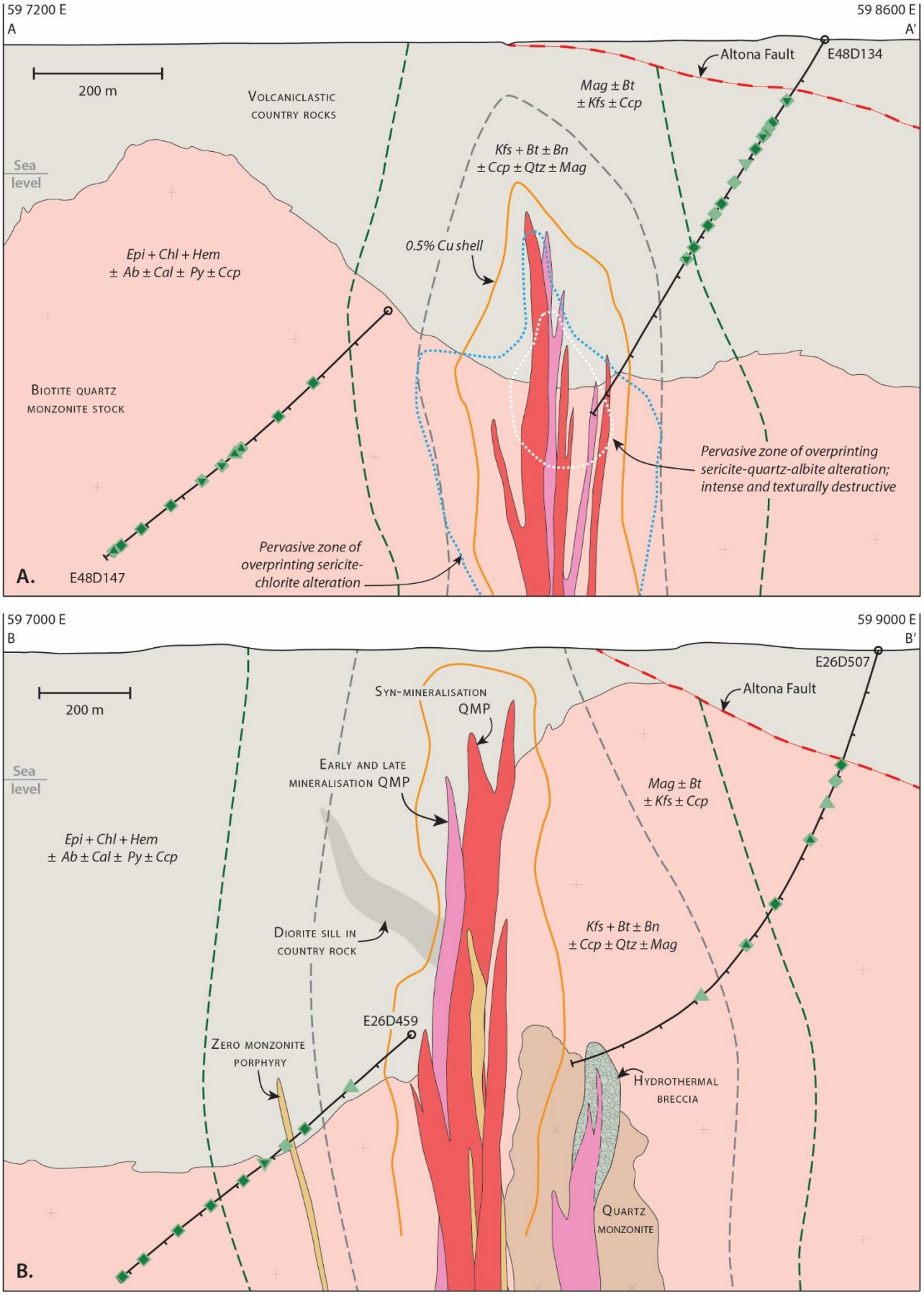
59 7200 E
A
59 8600 E
A'
200 m
Volcaniclastic country rocks
Altona Fault
E48D134
Mag ± Bt ± Kfs ± Ccp
Kfs + Bt ± Bn ± Ccp ± Qtz ± Mag
Sea level
Epi + Chl + Hem ± Ab ± Cal ± Py ± Ccp
0.5% Cu shell
Biotite quartz monzonite stock
Pervasive zone of overprinting sericite-quartz-albite alteration; intense and texturally destructive
Pervasive zone of overprinting sericite-chlorite alteration
E48D147
A.
59 7000 E
B
59 9000 E
B'
200 m
Syn-mineralisation QMP
E26D507
Altona Fault
Early and late mineralisation QMP
Sea level
Mag ± Bt ± Kfs ± Ccp
Epi + Chl + Hem ± Ab ± Cal ± Py ± Ccp
Diorite sill in country rock
Kfs + Bt ± Bn ± Ccp ± Qtz ± Mag
E26D459
Zero monzonite porphyry
Hydrothermal breccia
Quartz monzonite
B.

Figure 2

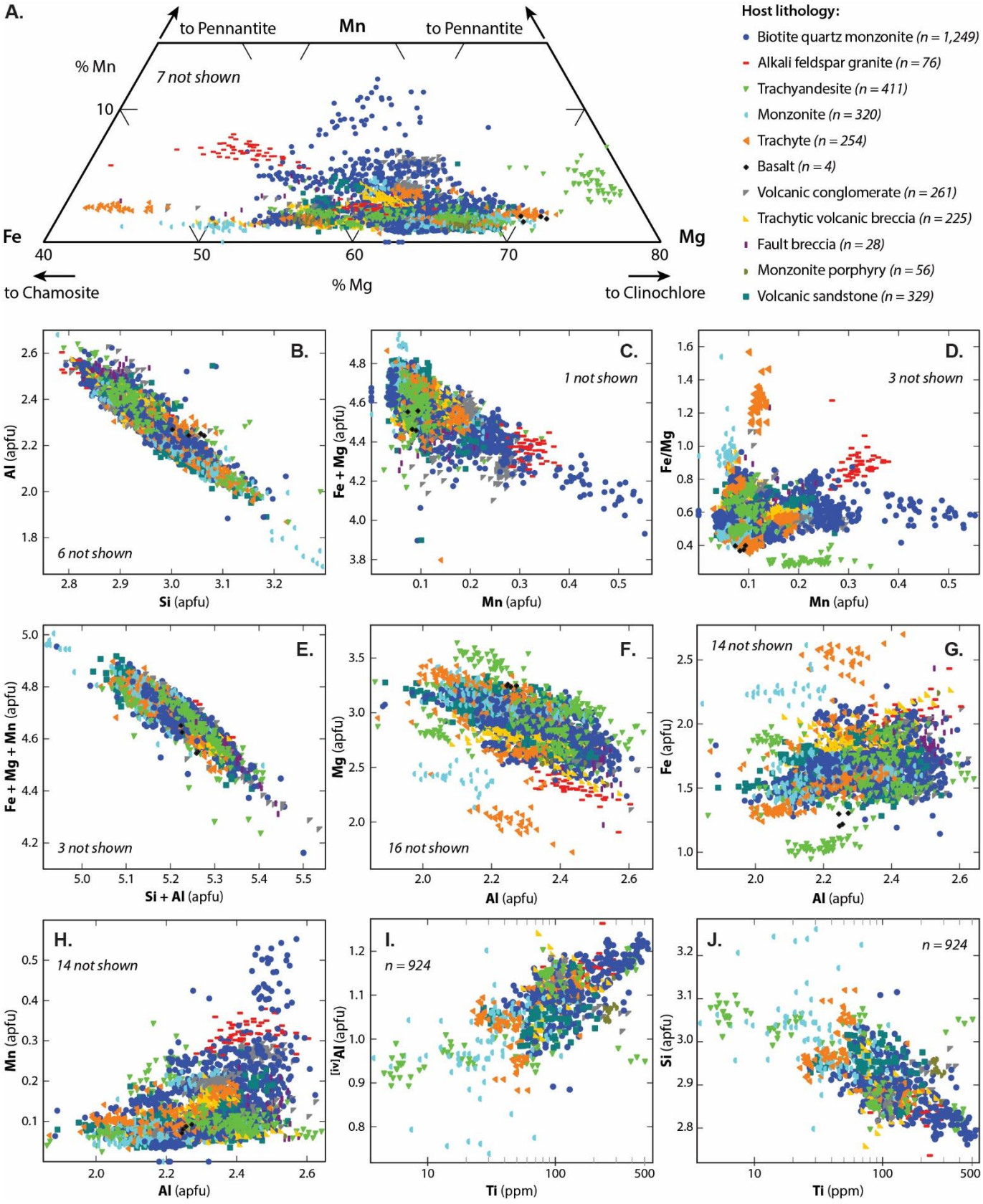
A.
to Pennantite
Mn
to Pennantite
% Mn
10
7 not shown
Fe
Mg
40
50
60
70
80
to Chamosite
% Mg
to Clinochlore
Host lithology:
Biotite quartz monzonite (n = 1,249)
Alkali feldspar granite (n = 76)
Trachyandesite (n = 411)
Monzonite (n = 320)
Trachyte (n = 254)
Basalt (n = 4)
Volcanic conglomerate (n = 261)
Trachytic volcanic breccia (n = 225)
Fault breccia (n = 28)
Monzonite porphyry (n = 56)
Volcanic sandstone (n = 329)
B.
6 not shown
Al (apfu)
Si (apfu)
C.
1 not shown
Fe + Mg (apfu)
Mn (apfu)
D.
3 not shown
Fe/Mg
Mn (apfu)
E.
3 not shown
Fe + Mg + Mn (apfu)
Si + Al (apfu)
F.
16 not shown
Mg (apfu)
Al (apfu)
G.
14 not shown
Fe (apfu)
Al (apfu)
H.
14 not shown
Mn (apfu)
Al (apfu)
I.
n = 924
[iv]Al (apfu)
Ti (ppm)
J.
n = 924
Si (apfu)
Ti (ppm)

Figure 3

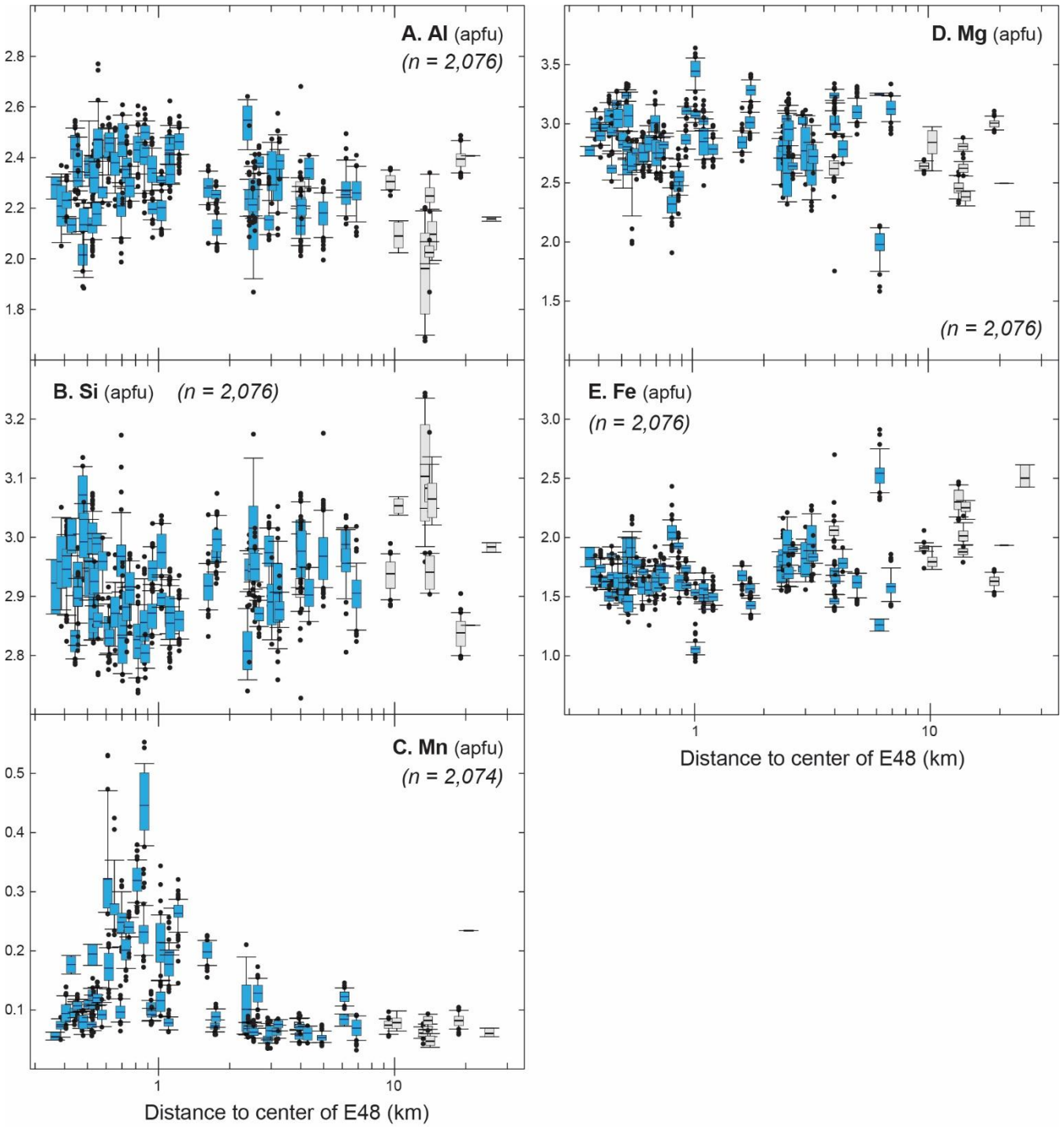
A. Al (apfu)
(n = 2,076)
B. Si (apfu) (n = 2,076)
C. Mn (apfu)
(n = 2,074)
D. Mg (apfu)
(n = 2,076)
E. Fe (apfu)
(n = 2,076)
Distance to center of E48 (km)
Distance to center of E48 (km)

Figure 4

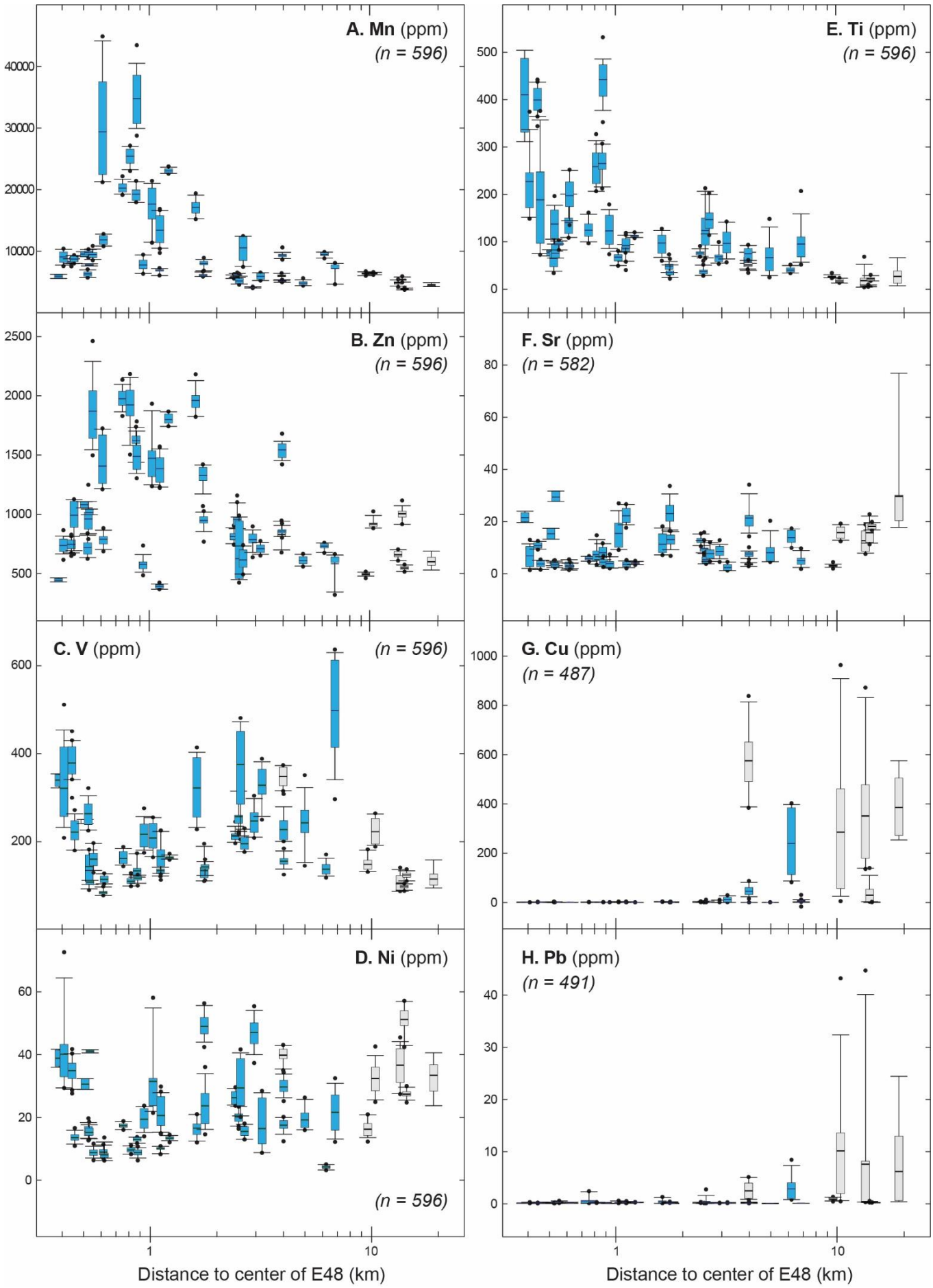
A. Mn (ppm)
(n = 596)
E. Ti (ppm)
(n = 596)
B. Zn (ppm)
(n = 596)
F. Sr (ppm)
(n = 582)
C. V (ppm)
(n = 596)
G. Cu (ppm)
(n = 487)
D. Ni (ppm)
(n = 596)
H. Pb (ppm)
(n = 491)
Distance to center of E48 (km)
Distance to center of E48 (km)

Figure 5

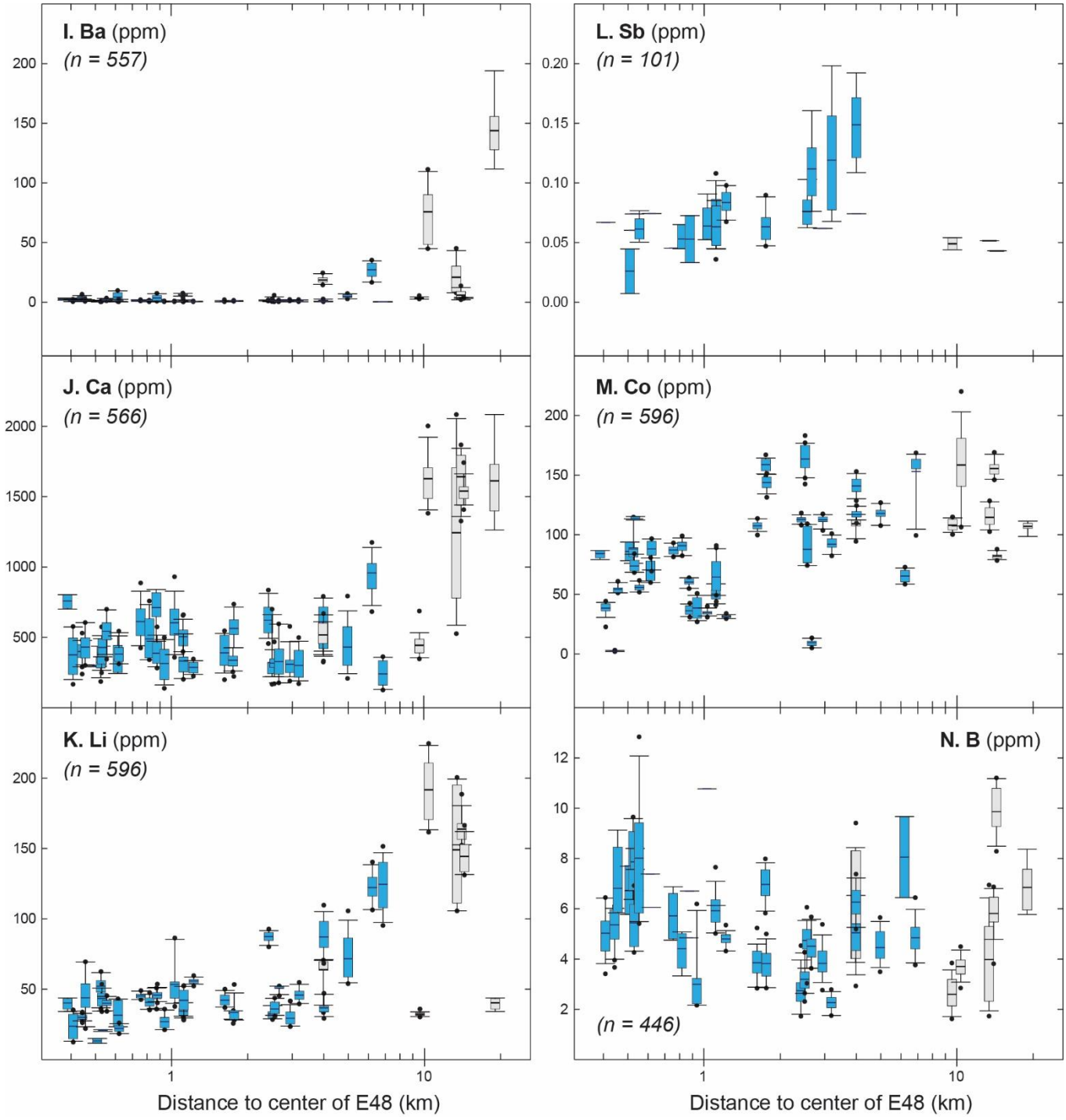
I. Ba (ppm)
(n = 557)
L. Sb (ppm)
(n = 101)
J. Ca (ppm)
(n = 566)
M. Co (ppm)
(n = 596)
K. Li (ppm)
(n = 596)
N. B (ppm)
(n = 446)
Distance to center of E48 (km)
Distance to center of E48 (km)

Figure 5

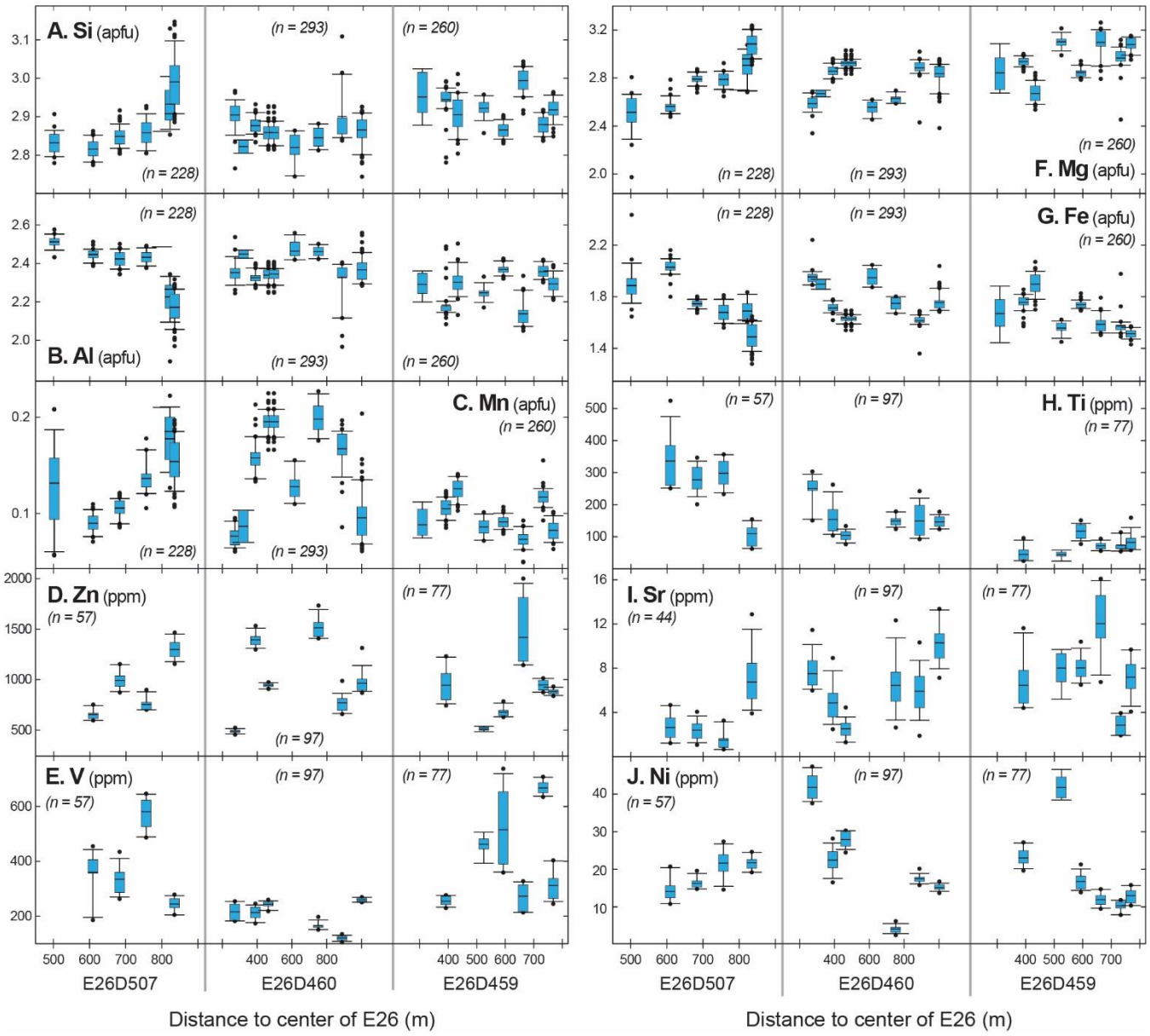
A. Si (apfu)
(n = 228)
(n = 293)
(n = 260)
B. Al (apfu)
C. Mn (apfu)
D. Zn (ppm)
(n = 57)
(n = 97)
(n = 77)
E. V (ppm)
F. Mg (apfu)
G. Fe (apfu)
H. Ti (ppm)
I. Sr (ppm)
(n = 44)
J. Ni (ppm)
E26D507
E26D460
E26D459
Distance to center of E26 (m)

Figure 6

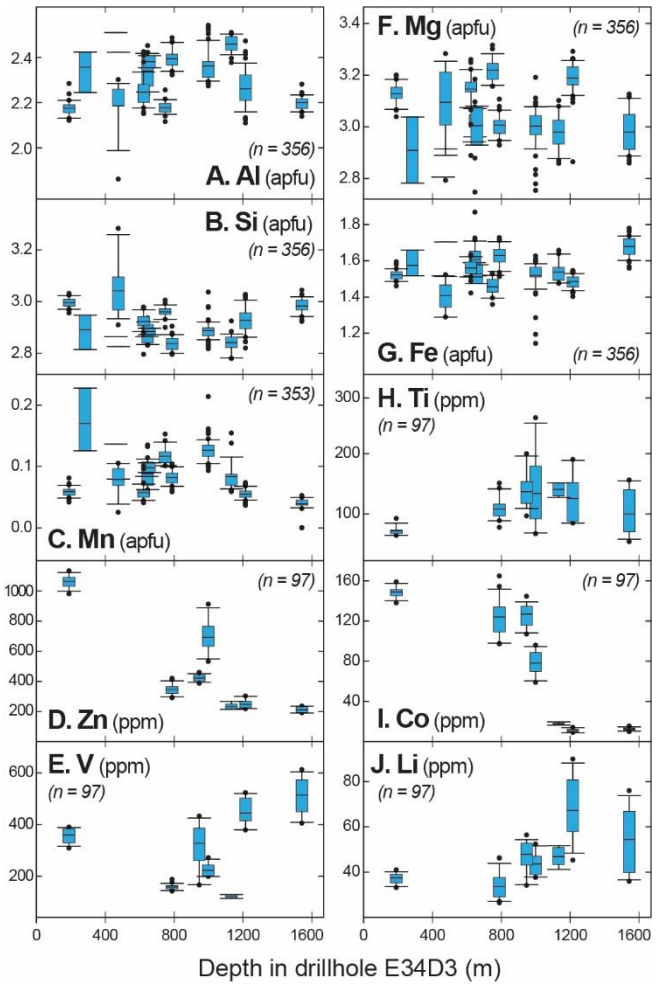
A. Al (apfu)
(n = 356)
B. Si (apfu)
(n = 356)
C. Mn (apfu)
(n = 353)
D. Zn (ppm)
(n = 97)
E. V (ppm)
(n = 97)
F. Mg (apfu)
(n = 356)
G. Fe (apfu)
(n = 356)
H. Ti (ppm)
(n = 97)
I. Co (ppm)
(n = 97)
J. Li (ppm)
(n = 97)
0
400
800
1200
1600
Depth in drillhole E34D3 (m)

Figure 7

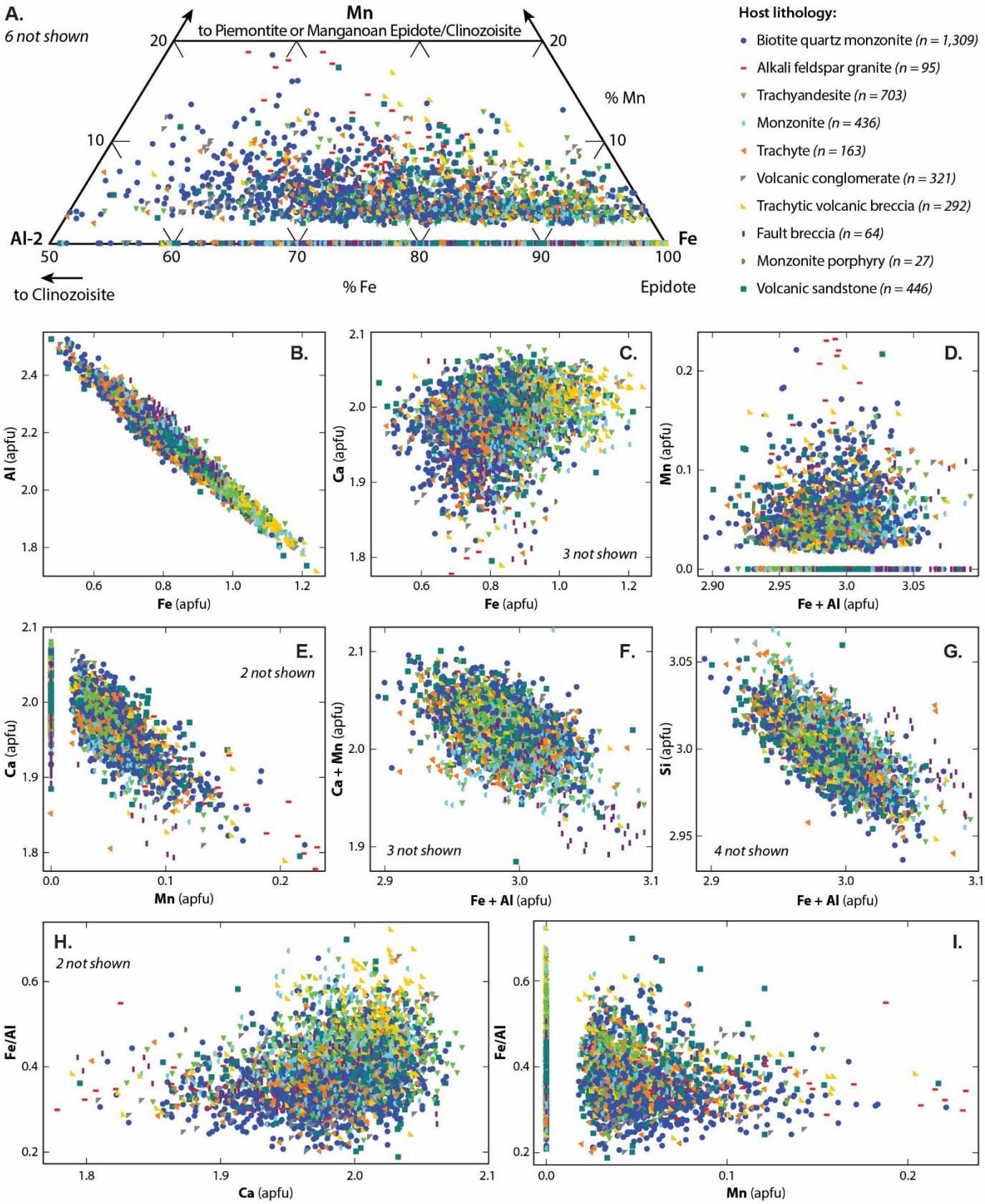
A.
6 not shown
Mn
to Piemontite or Manganoan Epidote/Clinozoisite
20
20
% Mn
10
10
Al-2
Fe
50
60
70
80
90
100
to Clinozoisite
% Fe
Epidote
Host lithology:
Biotite quartz monzonite (n = 1,309)
Alkali feldspar granite (n = 95)
Trachyandesite (n = 703)
Monzonite (n = 436)
Trachyte (n = 163)
Volcanic conglomerate (n = 321)
Trachytic volcanic breccia (n = 292)
Fault breccia (n = 64)
Monzonite porphyry (n = 27)
Volcanic sandstone (n = 446)
B.
Al (apfu)
Fe (apfu)
C.
3 not shown
Ca (apfu)
Fe (apfu)
D.
Mn (apfu)
Fe + Al (apfu)
E.
2 not shown
Ca (apfu)
Mn (apfu)
F.
3 not shown
Ca + Mn (apfu)
Fe + Al (apfu)
G.
4 not shown
Si (apfu)
Fe + Al (apfu)
H.
2 not shown
Fe/Al
Ca (apfu)
I.
Fe/Al
Mn (apfu)

Figure 8

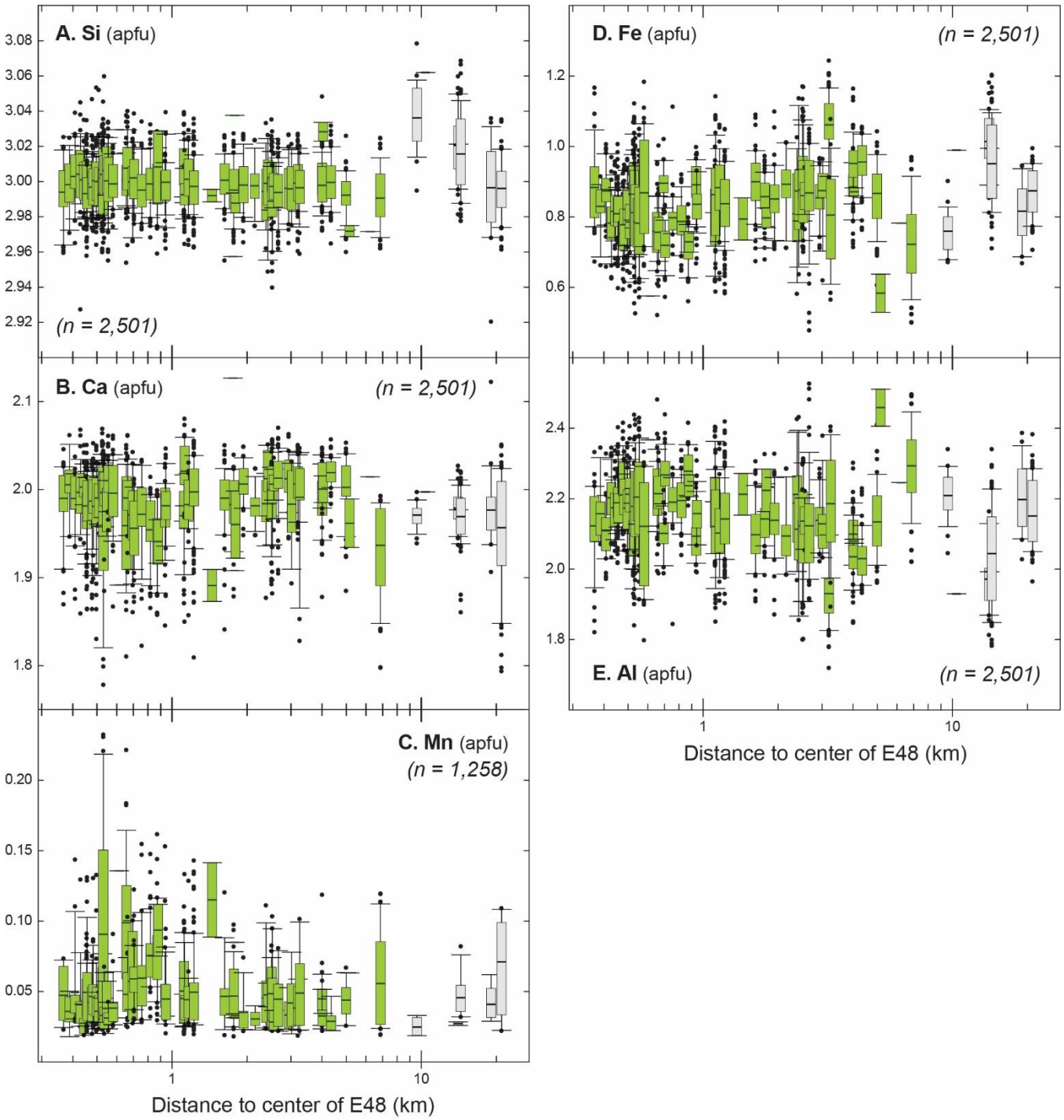
A. Si (apfu)
(n = 2,501)
B. Ca (apfu)
(n = 2,501)
C. Mn (apfu)
(n = 1,258)
D. Fe (apfu)
(n = 2,501)
E. Al (apfu)
(n = 2,501)
Distance to center of E48 (km)
Distance to center of E48 (km)

Figure 9

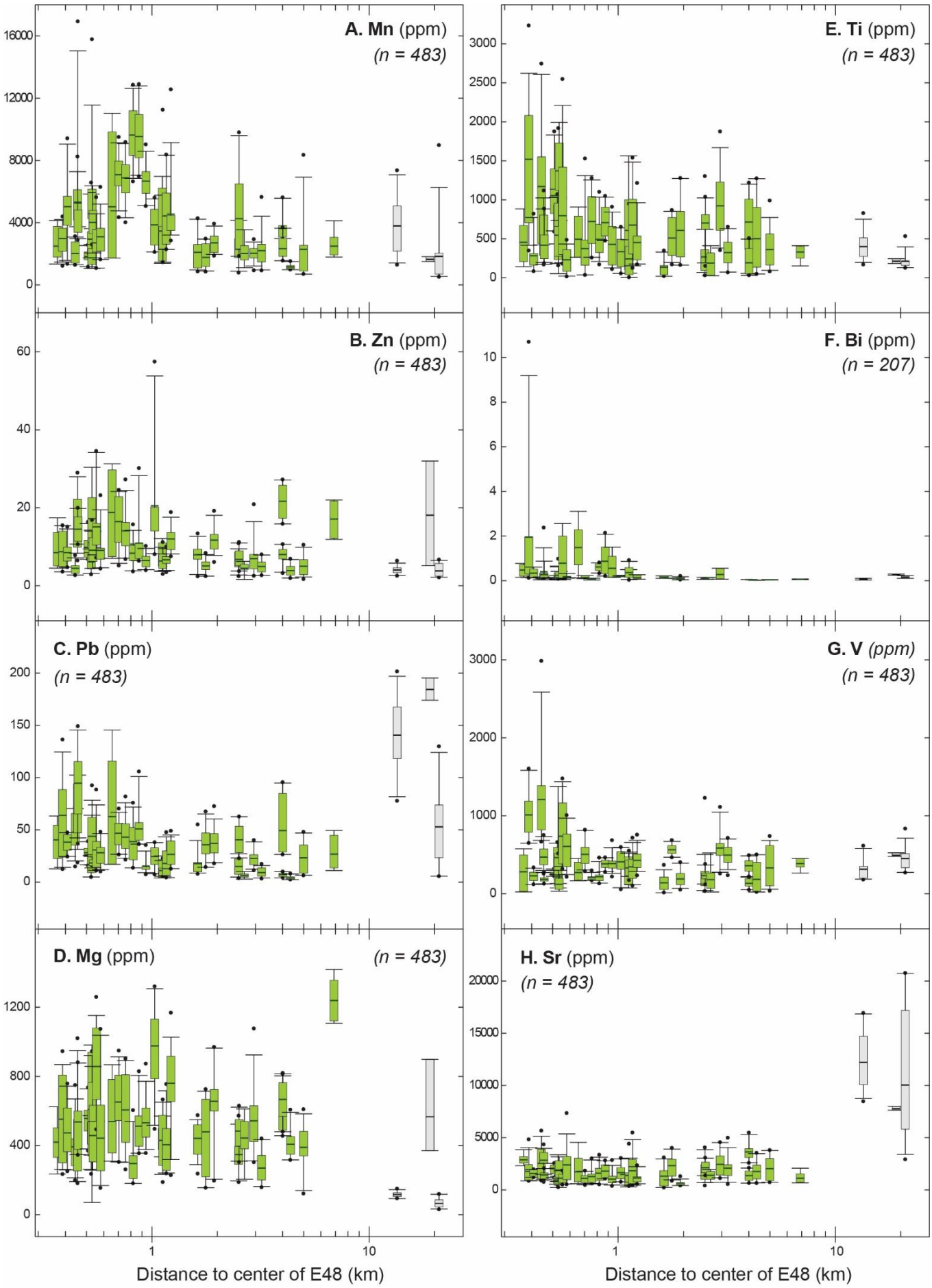
A. Mn (ppm)
(n = 483)
E. Ti (ppm)
(n = 483)
B. Zn (ppm)
(n = 483)
F. Bi (ppm)
(n = 207)
C. Pb (ppm)
(n = 483)
G. V (ppm)
(n = 483)
D. Mg (ppm)
(n = 483)
H. Sr (ppm)
(n = 483)
Distance to center of E48 (km)
Distance to center of E48 (km)

Figure 10

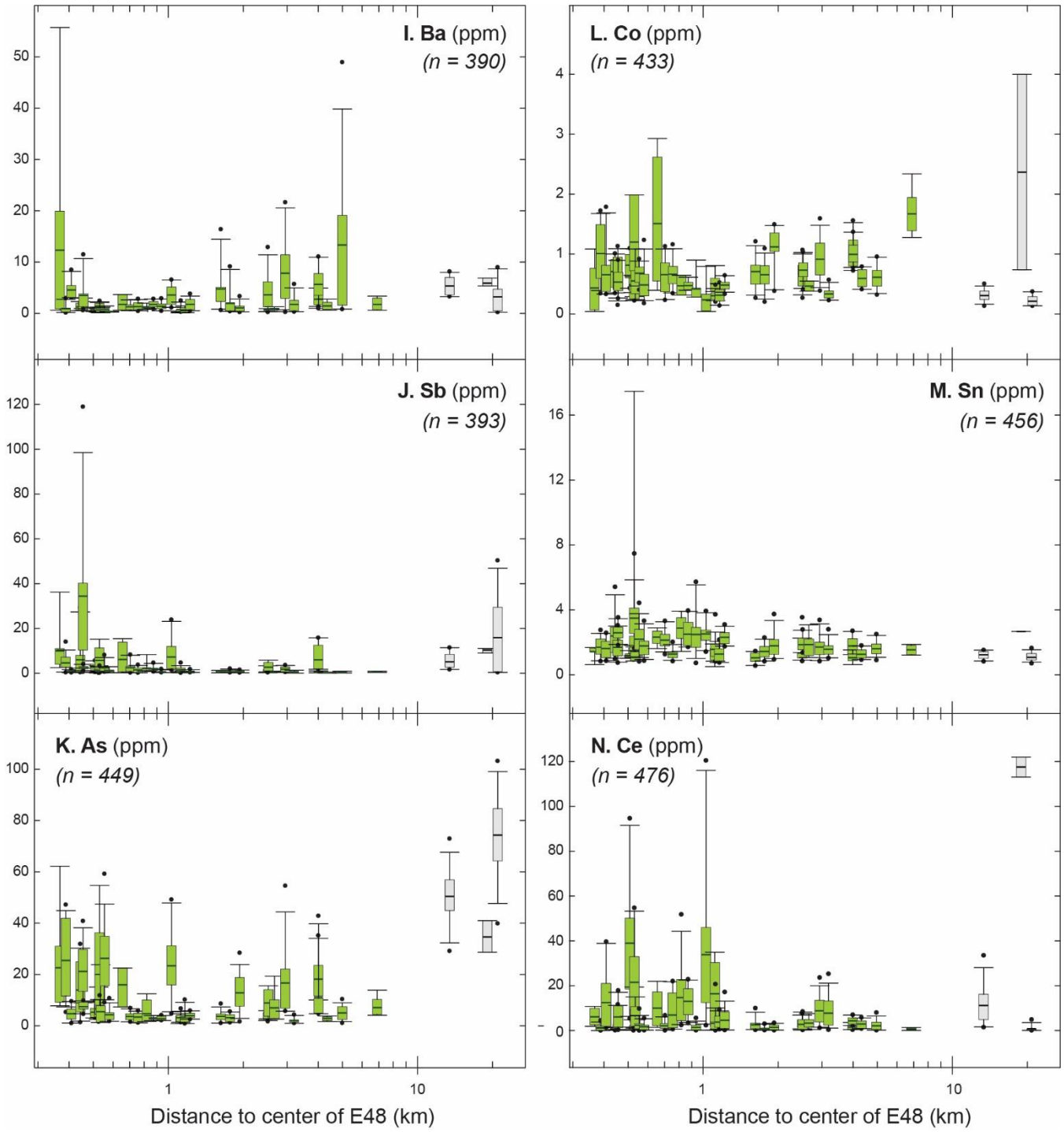
I. Ba (ppm)
(n = 390)
L. Co (ppm)
(n = 433)
J. Sb (ppm)
(n = 393)
M. Sn (ppm)
(n = 456)
K. As (ppm)
(n = 449)
N. Ce (ppm)
(n = 476)
Distance to center of E48 (km)
Distance to center of E48 (km)

Figure 10

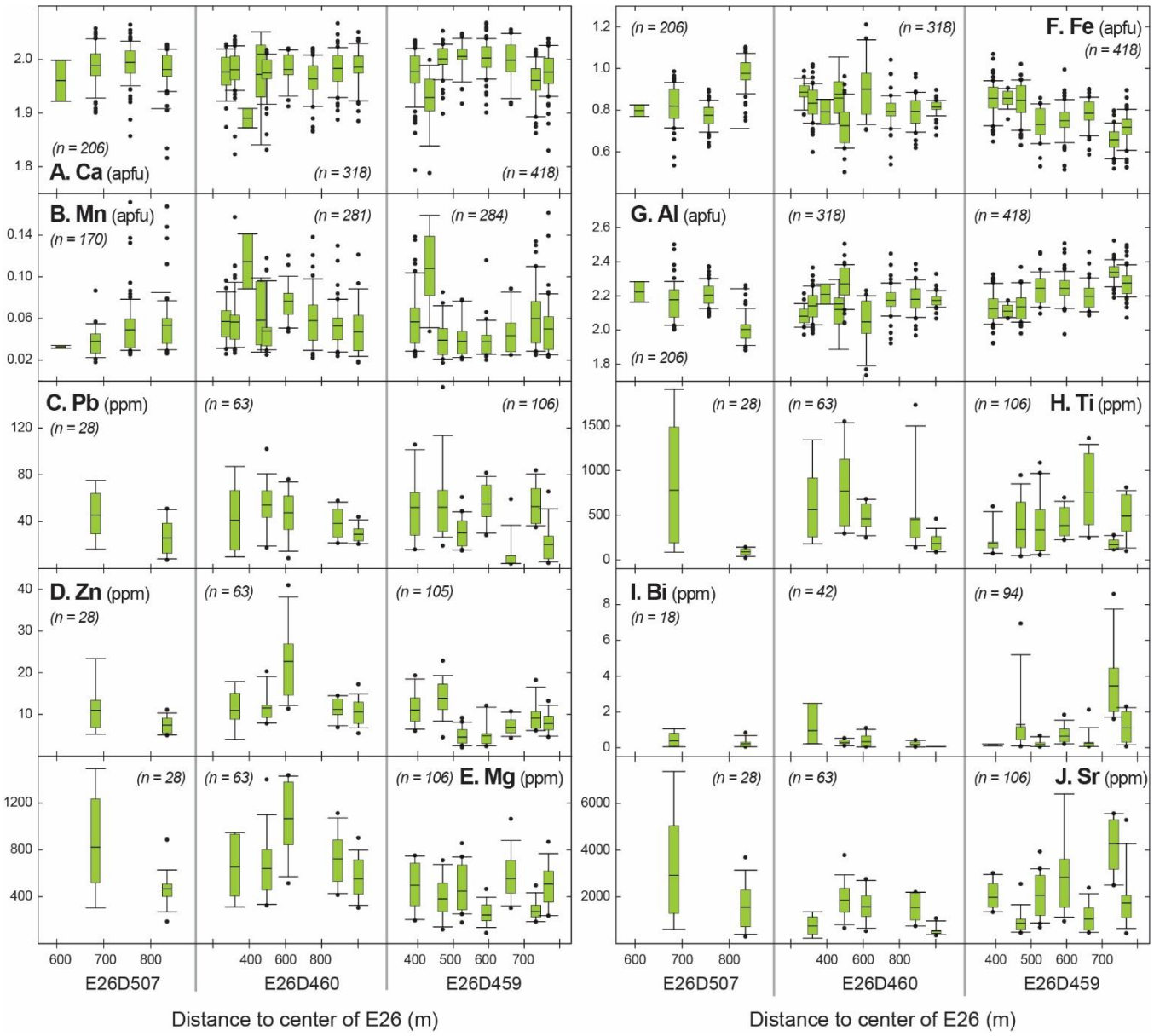
A. Ca (apfu)
B. Mn (apfu)
C. Pb (ppm)
D. Zn (ppm)
E. Mg (ppm)
F. Fe (apfu)
G. Al (apfu)
H. Ti (ppm)
I. Bi (ppm)
J. Sr (ppm)
E26D507
E26D460
E26D459
Distance to center of E26 (m)

Figure 11

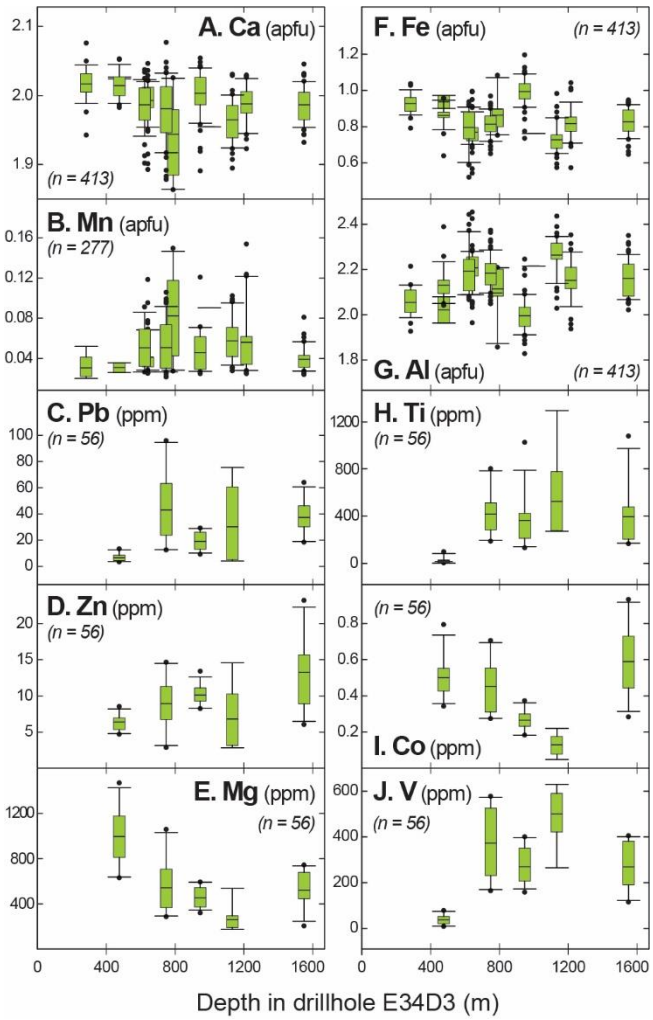
A. Ca (apfu)
(n = 413)
F. Fe (apfu)
(n = 413)
B. Mn (apfu)
(n = 277)
G. Al (apfu)
(n = 413)
C. Pb (ppm)
(n = 56)
H. Ti (ppm)
(n = 56)
D. Zn (ppm)
(n = 56)
(n = 56)
I. Co (ppm)
E. Mg (ppm)
(n = 56)
J. V (ppm)
(n = 56)
Depth in drillhole E34D3 (m)

Figure 12

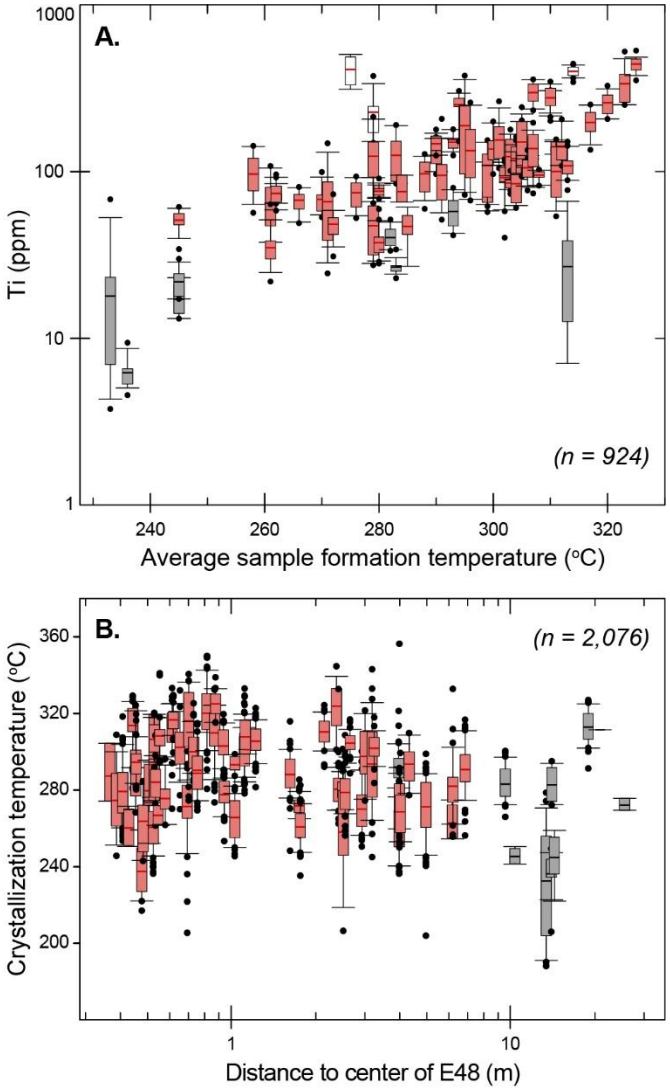
A.
1000
100
10
1
Ti (ppm)
(n = 924)
240
260
280
300
320
Average sample formation temperature (°C)
B.
(n = 2,076)
360
320
280
240
200
Crystallization temperature (°C)
1
10
Distance to center of E48 (m)

Figure 13